https://doi.org/10.5194/egusphere-2026-4386
Preprint. Discussion started: 4 August 2026

Transient electroosmotic transport under evolving pH and contrasting background electrolyte concentrations: coupled controls of interfacial charge and pore structure

Wencheng Wu[1,2], Guofang Pan[1,2], Heng Dai[3,4], Jing Yang[5], and Ping Yang[1,2]

[1]South China Institute of Environmental Sciences, Ministry of Ecology and Environment (MEE), Guangzhou, Guangdong 510655, China
[2]State Environmental Protection Key Laboratory of Water Environment Simulation and Pollution Control, MEE, Guangzhou, Guangdong 510530, China
[3]State Key Laboratory of Geomicrobiology and Environmental Changes, China University of Geosciences, Wuhan, Hubei 430074, China
[4]Hubei Key Laboratory of Yangtze Catchment Environmental Aquatic Science, China University of Geosciences, Wuhan, Hubei 430074, China
[5]School of Land Engineering, Chang'an University, Xi'an, Shaanxi 710054, China

Correspondence to: Ping Yang (yangping@scies.org)

Abstract. Electroosmotic flow (EOF) can transport porewater and dissolved neutral solutes through fine-grained porous media, but its magnitude may evolve as electrode reactions alter pH and electrolyte conditions at mineral–water interfaces. Here, we use 24 two-dimensional pore-scale simulations to quantify how interfacial-charge parameterization, background electrolyte concentration, and pore architecture regulate transient electroosmotic displacement. The model couples incompressible flow, multicomponent Nernst–Planck–Poisson transport, time-dependent electrolysis boundary forcing, and chemistry-dependent electroosmotic slip. Zeta potential is calculated from the local aqueous chemistry using either a one-pK electric-double-layer (EDL) parameterization or a two-pK extended triple-layer (ETL) parameterization. The simulations were conducted in four uniformly oriented packings and two composite pore geometries. Under a matched background electrolyte concentration of 10 mM, the geometry-averaged fraction of tracer depleted from the contaminated medium zone after 30 min was 0.998 for the EDL cases and 0.918 for the ETL cases, while the corresponding late-time tailing indices were 0.002 and 0.094. Within the ETL cases, increasing the background electrolyte concentration from 1 to 100 mM reduced the mean 30 min depletion fraction from 0.963 to 0.613 and increased the tailing index from 0.037 to 0.465. None of the 100 mM cases reached 90 % depletion within 30 min. Pore architecture did not alter this group-level ordering but systematically reorganized directional transport and plume geometry within each electrochemical regime. In the uniformly oriented packings, rotation redistributed flow between the gradient-aligned and transverse directions and produced systematic plume reorientation, although fixed-time depletion varied non-monotonically with angle. In the composite geometries, the heterogeneous directional geometry maintained stronger domain-scale directional organization and reached its case-specific early and intermediate progress levels earlier than the non-directional geometry, whereas their fixed-window depletion ranking depended on the electrochemical setting. Comparisons at case-specific relative progress levels separated plume reorganization from differences in transport timescale.

https://doi.org/10.5194/egusphere-2026-4386
Preprint. Discussion started: 4 August 2026

These results reveal a two-level control on transient electroosmotic transport: interfacial-charge representation and background electrolyte concentration determine transport magnitude and timescale, whereas pore structure redistributes flow pathways and plume geometry within the resulting regime.

1 Introduction

Organic contaminants can persist in fine-grained soils and sediments because low hydraulic conductivity restricts pressure-driven flushing, leaving molecular diffusion as a dominant transport mechanism (Souza et al., 2017; Li and Yu, 2015; Gill et al., 2014; Yeung and Gu, 2011; Yeung and Datla, 1995; Qin et al., 2015; Xu et al., 2019; Chowdhury et al., 2017). Electrokinetic remediation provides an alternative mechanism for inducing porewater movement. When an electric field is applied across a charged porous medium, electroosmotic flow (EOF) develops along mineral surfaces and can advect porewater and dissolved neutral solutes through pore spaces in which pressure-driven flow is inefficient (Qiao et al., 2018; Shi et al., 2008; Ko et al., 2000; Shapiro and Probstein, 1993; Sprocati et al., 2020).

Electroosmotic mobility is not necessarily constant during electrokinetic treatment. Water electrolysis generates acidic conditions near the anode and alkaline conditions near the cathode, while electromigration redistributes dissolved ions and alters local electrolyte composition. These chemical changes modify mineral–water interfacial charge and the zeta potential, ζ, which controls electroosmotic slip (Acar and Alshawabkeh, 1993; Shapiro and Probstein, 1993; Revil, 2017; Zhang and Wang, 2015, 2017; Eykholt and Daniel, 1994; Dzenitis, 1997). Consequently, both the magnitude and spatial distribution of EOF may evolve during treatment, producing non-uniform solute displacement and persistent residual concentrations (Crespy et al., 2007; Masi et al., 2017; Thormann et al., 1998; Sprocati et al., 2020; Sun et al., 2019; Rezaee et al., 2019; Lopez-Vizcaino et al., 2017).

Pore-scale models commonly represent this coupling by relating zeta potential to local aqueous chemistry and applying the resulting electroosmotic mobility through a slip boundary condition (Yang et al., 2022; de Lima et al., 2010a; de Lima et al., 2010b; Zhang and Wang, 2017). This approach allows spatially and temporally varying aqueous chemistry to affect pore-scale flow without explicitly resolving the electric double layer. However, the predicted response depends on the constitutive representation of interfacial charge. A one-pK electric-double-layer (EDL) parameterization primarily describes proton-regulated surface charging, whereas a two-pK extended triple-layer (ETL) parameterization additionally represents distinct protonation and deprotonation reactions, specific cation adsorption, and charge partitioning among interfacial planes (Wang and Revil, 2010). These formulations may therefore predict substantially different transient EOF responses, particularly at elevated electrolyte concentrations. Few pore-scale studies, however, have compared alternative interfacial-charge formulations and pore architectures within a common numerical framework, making their respective effects on transient transport difficult to separate.

Pore architecture provides an additional control on electroosmotic transport. Particle orientation changes the alignment of mineral surfaces with the imposed electric field, whereas composite media introduce internal structural contrasts, constrictions,

https://doi.org/10.5194/egusphere-2026-4386
Preprint. Discussion started: 4 August 2026

and alternative transport pathways. Previous studies have shown that pore geometry affects electrokinetic velocity, mixing, and dispersion even under similar externally imposed electrical conditions (Godinez-Brizuela and Niasar, 2020; Alizadeh et al., 2019; Hlushkou et al., 2007). Bulk displacement metrics and mean velocities alone may therefore be insufficient to characterize structural effects (Eykholt and Daniel, 1994; Crespy et al., 2007; Masi et al., 2017). Plume position, orientation, spreading, and residual-concentration patterns are also needed to determine whether similar bulk responses arise from different pore-scale pathways.

These considerations motivate three questions. First, how do the selected one-pK and two-pK interfacial-charge parameterizations differ in their predictions of transient electroosmotic displacement under matched background electrolyte conditions? Second, how does background electrolyte concentration affect displacement within the extended triple-layer formulation? Third, under fixed interfacial conditions, how does pore architecture redistribute directional flow, alter plume geometry, and affect transport timing and persistence? From a hydrological perspective, the underlying issue is whether electroosmotically driven porewater flow can be represented using a fixed mobility or must instead be treated as a transient flow regulated by evolving aqueous chemistry and spatially redistributed by pore architecture. We address these questions by combining bulk depletion and persistence metrics with spatial plume descriptors evaluated at case-specific relative progress levels. Figure 1 summarizes the conceptual distinction between the two controls: the interfacial parameterization translates local aqueous chemistry into zeta potential and electroosmotic mobility, whereas pore architecture governs how the resulting flow is distributed through the pore space.

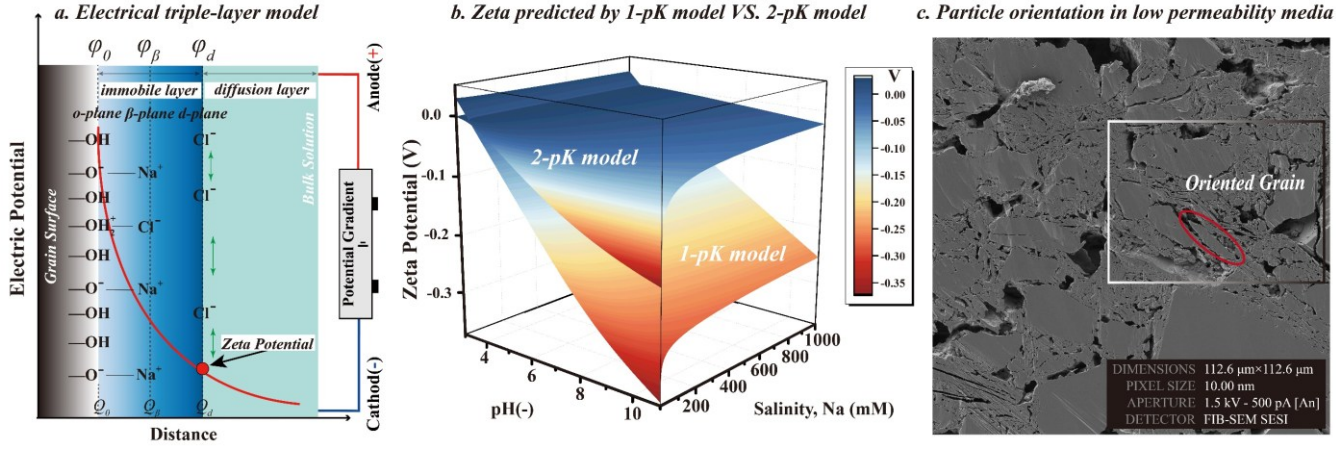

Figure 1. Conceptual controls on transient electroosmotic transport.

(a) Schematic representation of the extended triple-layer structure and the shear-plane zeta potential at elevated electrolyte concentration. (b) Illustrative zeta-potential responses calculated using the one-pK EDL and two-pK ETL parameterizations described in Sect. S1. (c) Representative focused-ion-beam scanning electron microscopy (FIB–SEM) image illustrating particle orientation and structural heterogeneity in a fine-grained porous medium. Panels (b) and (c) provide conceptual and structural context and are neither direct simulation outputs nor geometries used as inputs to the pore-scale simulations.

To examine these controls, we conducted 24 two-dimensional pore-scale simulations coupling incompressible flow, multicomponent ionic transport, electric potential, electrolysis-driven boundary chemistry, and chemistry-dependent

https://doi.org/10.5194/egusphere-2026-4386
Preprint. Discussion started: 4 August 2026

electroosmotic slip. The simulations span four uniformly oriented elliptical packings and two composite pore geometries under controlled electrochemical conditions. The SROE series provides a controlled test of how progressive packing rotation redistributes electroosmotic flow and reorganizes plume geometry, whereas the HD–ND comparison contrasts directional composite organization with non-directional grain-size heterogeneity. The design supports two complementary electrochemical comparisons: the two interfacial-charge parameterizations are evaluated under a common background electrolyte condition, while electrolyte-concentration effects are examined within the ETL formulation. Applying the same suite of pore geometries across these comparisons allows the effects of pore architecture on flow partitioning and plume organization to be evaluated within each electrochemical setting. Together, this framework links evolving boundary chemistry to interfacial electrokinetics and structure-dependent solute transport in low-permeability porous media, thereby clarifying how chemically regulated electroosmotic water movement contributes to advective transport where pressure-driven flow is weak.

2 Methods

We performed two-dimensional pore-scale simulations to examine how the interfacial-charge parameterization, background electrolyte concentration, and pore architecture control transient electroosmotic transport. The model couples incompressible fluid flow, multicomponent ion transport, electric potential, and time-dependent electrolysis boundary forcing. The zeta potential at each solid–liquid interface is updated from the adjacent aqueous composition and incorporated into an electroosmotic slip boundary condition. The following sections describe the governing equations, interfacial parameterizations, pore geometries, numerical implementation, boundary and initial conditions, and transport diagnostics.

2.1 Pore-scale electrokinetic transport model

The model represents the coupled evolution of aqueous chemistry and electroosmotic transport. Water electrolysis modifies the distributions of H^+ and OH^- within the pore space, while electromigration and advection redistribute the background electrolyte. The resulting local pH and electrolyte conditions determine the zeta potential, ζ, at mineral–water interfaces. The zeta potential controls electroosmotic mobility and the corresponding tangential slip velocity along grain surfaces. The resulting porewater flow, in turn, transports dissolved ions and the neutral tracer. The model therefore couples electrolysis-driven aqueous chemistry, chemistry-dependent interfacial slip, and pore-scale solute transport through the interfacial-charge relations, multicomponent transport equations, and time-dependent electrode boundary conditions described below.

2.1.1 Zeta-potential closures

The zeta potential is evaluated at each solid–liquid boundary using one of two equilibrium interfacial parameterizations: a one-pK electric-double-layer (EDL) formulation and a two-pK extended triple-layer (ETL) formulation. The one-pK EDL formulation represents proton-regulated charging of an amphoteric surface site and relates the interfacial electrokinetic state

https://doi.org/10.5194/egusphere-2026-4386
Preprint. Discussion started: 4 August 2026

primarily to local proton concentration and ionic strength (de Lima et al., 2010b; Zhang and Wang, 2017). The two-pK ETL formulation separately represents surface protonation and deprotonation, specific adsorption of the background cation, and charge partitioning among the surface, Stern, and diffuse-layer planes. It therefore provides a more explicit representation of the dependence of ζ on both pH and electrolyte concentration (Wang and Revil, 2010).

The parameter set defines a quartz-like reference surface for controlled model comparison. Values for surface-site density, point of zero charge, equilibrium constants, and Stern-layer capacitances were compiled from the cited studies and applied consistently across all simulations (Wang and Revil, 2010; Zhang and Zhang, 1992; Bray et al., 2014; Liu et al., 2013; Leroy et al., 2007; Papirer, 2000). The governing interfacial equations and parameter values are provided in Sect. S1 and Table S1. Under the local-equilibrium assumption, the interfacial equations update ζ pointwise from the aqueous conditions adjacent to each grain surface, and the resulting value determines the local electroosmotic mobility in the slip boundary condition. The two formulations therefore serve as chemistry-dependent constitutive relations for electroosmotic slip. Surface speciation determines the interfacial electrokinetic state, but finite surface-site inventories and associated surface-reaction source or sink terms are not included in the aqueous species balances.

2.1.2 Flow and electroosmotic slip

The porewater is treated as an incompressible Newtonian fluid. The full incompressible Navier–Stokes equations are retained in the numerical implementation, although the simulated velocities and characteristic pore dimensions correspond to a low-Reynolds-number regime. Conservation of mass and momentum is expressed as

$$\nabla \cdot \boldsymbol{u} = 0 \,, \tag{1}$$

$$\rho \frac{\partial \boldsymbol{u}}{\partial t} + \rho(\boldsymbol{u} \cdot \nabla)\boldsymbol{u} = \nabla \cdot [-p\bar{\boldsymbol{I}} + \mu(\nabla \boldsymbol{u} + (\nabla \boldsymbol{u})^{\mathrm{T}})] + \boldsymbol{F} \,. \tag{2}$$

Here, ρ (kg·m^{-3}) is the fluid density, $\boldsymbol{u}$ (m·s^{-1}) is the velocity vector, p (Pa) is pressure, μ (Pa·s) is the dynamic viscosity, $\bar{\boldsymbol{I}}$ is the identity tensor, and $\boldsymbol{F}$ (N·m^{-3}) is the volumetric body-force term. In the present simulations, $\boldsymbol{F} = 0$, because electroosmotic forcing is represented through a thin-double-layer slip condition at the solid–liquid boundary rather than by an electrical body force explicitly resolved within the porewater (Appelo, 2017; Yang and Wang, 2019; Alizadeh et al., 2019; Peters et al., 2016; Alizadeh et al., 2017; Godinez-Brizuela and Niasar, 2020).

Electroosmotic slip at the grain surface is represented by the Helmholtz–Smoluchowski relation

$$\boldsymbol{u}_{eo} = \mu_{eo}\boldsymbol{E}_t = \frac{\varepsilon_0 \varepsilon_r \zeta}{\mu}(\bar{\boldsymbol{I}} - \boldsymbol{nn}) \cdot \nabla \Phi \,, \tag{3}$$

where $\mu_{eo} = -\varepsilon_0 \varepsilon_r \zeta / \mu$ (m^2·V^{-1}·s^{-1}) is the electroosmotic mobility, ε_0 (F·m^{-1}) is the vacuum permittivity, ε_r (–) is the relative permittivity of the aqueous phase, $\boldsymbol{n}$ is the outward unit normal to the grain surface, $\boldsymbol{E}_t$ (V·m^{-1}) is the tangential electric field, and Φ (V) is the electric potential. The normal fluid velocity at grain surfaces is zero, while the tangential velocity is prescribed by Eq. (3). The resulting velocity field is used as the advective velocity for all aqueous species.

https://doi.org/10.5194/egusphere-2026-4386
Preprint. Discussion started: 4 August 2026

2.1.3 Multicomponent transport and electric potential

Transport of each aqueous species is described by the Nernst–Planck flux, which includes molecular diffusion, electromigration, and advection:

$$\boldsymbol{J}_i = -D_i \nabla C_i - D_i C_i \frac{z_i F}{RT} \nabla \Phi + \boldsymbol{u} C_i \,, \tag{4}$$

where $\boldsymbol{J}_i$(mol·m^{-2}·s^{-1}) is the flux of species i. Mass conservation for species i is expressed as

$$\frac{\partial C_i}{\partial t} + \nabla \cdot \boldsymbol{J}_i = R_i \,, \tag{5}$$

where D_i (m^2·s^{-1}), C_i (mol·m^{-3}), and z_i (–) are the molecular diffusion coefficient, molar concentration, and charge number of species i, respectively; F (C·mol^{-1}) is the Faraday constant; R (J·mol^{-1}·K^{-1}) is the universal gas constant; T (K) is the absolute temperature; and R_i (mol·m^{-3}·s^{-1}) is the aqueous production or consumption rate. For the neutral tracer Org, $z_{\mathrm{Org}} = 0$, and the electromigration term in Eq. (4) therefore vanishes. Within the porewater domain, $R_i = 0$ for the transported species; water autoionization is imposed as an equilibrium constraint, and electrolysis is represented through boundary fluxes rather than volumetric reaction terms.

The electric potential is obtained from Poisson's equation

$$\nabla^2 \Phi = -\frac{\rho_e}{\varepsilon_0 \varepsilon_r} \,, \tag{6}$$

where $\rho_e = F \sum z_i C_i$ is the local aqueous charge density (C·m^{-3}). Equations (4)–(6), together with the flow equations and interfacial slip condition, describe the coupled evolution of aqueous concentrations, electric potential, and electroosmotic transport (Sun et al., 2019; Sprocati et al., 2021). The porewater electric potential and aqueous charge density are resolved at the pore scale, whereas the interfacial electric double layer is not explicitly meshed and is represented through the slip condition in Eq. (3).

2.1.4 Electrode reactions and pH forcing

Water electrolysis was represented as the only electrode process. The standard reduction half-reactions are given in Reactions (R1) and (R2). At the anode, Reaction (R1) proceeds in the reverse direction, producing H^+, whereas at the cathode, Reaction (R2) proceeds in the forward direction, producing OH^-. These reactions impose time-dependent acidic and alkaline forcing at the lateral boundaries and generate pH gradients across the pore space (Sprocati et al., 2019; Vizcaino et al., 2018; Cang et al., 2013; Xu et al., 2020):

$$O_2 + 4H^+ + 4e^- \rightleftharpoons 2H_2O \qquad E^0 = 1.229\,\mathrm{V} \,, \tag{R1}$$

$$2H_2O + 2e^- \rightleftharpoons H_2 + 2OH^- \qquad E^0 = -0.8277\,\mathrm{V} \,. \tag{R2}$$

https://doi.org/10.5194/egusphere-2026-4386
Preprint. Discussion started: 4 August 2026

The production fluxes of H^+ and OH^- are determined from the normal ionic current density according to Faraday's law. The concentrations in the idealized, well-mixed electrode chambers are then updated through boundary mass balances and imposed as spatially uniform, time-dependent concentration conditions at the anode and cathode boundaries. The ionic-current expressions, electrode-chamber mass balances, and species-specific boundary conditions are provided in Sect. S2 and Table S2.

Electrode chemistry and electroosmotic transport are dynamically coupled within the modelled aqueous system. Changes in proton concentration modify ζ and hence the electroosmotic slip velocity, while the resulting flow transports H^+, OH^-, and the background ions through the pore space. The electrode boundary conditions evolve together with the transport solution rather than being prescribed as fixed pH values. Accordingly, the modelled feedback links aqueous chemistry, the constitutive interfacial electrokinetic state, and porewater transport, while finite surface-site inventories and associated surface-reaction source terms are not included in the aqueous species balances.

2.2 Pore geometries and simulation design

2.2.1 Pore geometries

Two classes of two-dimensional pore geometries were constructed to distinguish orientation-associated structural effects from those arising from composite heterogeneity (Fig. 2). Each geometry consists of a central porous test section 2.0×10^{-3} m in length, flanked by an anode-side and a cathode-side buffer zone, each 2.5×10^{-4} m in length. These buffer zones separate the electrode boundaries from the porous medium and provide a consistent transition between the imposed electrochemical boundary conditions and transport within the pore space.

The first geometry class consists of regularly arranged elliptical grains with a uniform orientation. The entire packing was rotated clockwise by 0°, 15°, 30°, or 45°, while the grain dimensions and packing topology remained unchanged. Each ellipse has a semi-minor axis of 5.0×10^{-5} m and a semi-major axis of 1.0×10^{-4} m, giving porosities ranging from 0.35 to 0.40. These single-row oriented-ellipse (SROE) packings provide a controlled framework for evaluating transport differences associated with packing rotation while limiting changes in grain-size distribution and packing topology. Because packing rotation also introduces modest differences in porosity and local pore geometry, these comparisons are described throughout as orientation-associated structural effects. The SROE series was used to determine whether progressive structural rotation produces systematic changes in directional flow partitioning and plume geometry, and whether the corresponding CMZ depletion response varies monotonically with packing angle.

The second geometry class comprises two composite pore geometries. The non-directional composite (ND) was generated from a truncated lognormal grain-size distribution with a mean grain diameter of 5.0×10^{-5} m, a standard deviation of 1.5×10^{-5} m, and a target porosity of 0.35 following Yang et al. (2022). The heterogeneous directional geometry (HD) was constructed by combining subdomains containing SROE packings with different prescribed orientations. Unlike the SROE geometries, ND introduces grain-size variability without a preferred orientation, whereas HD combines orientation contrasts with internal

https://doi.org/10.5194/egusphere-2026-4386
Preprint. Discussion started: 4 August 2026

interfaces. These deterministic geometries provide controlled contrasts between non-directional grain-size variability and directional composite organization. The HD–ND comparison was used to assess whether directional subdomain organization produces more persistent domain-scale flow deflection and a transport-timing response distinct from that associated with non-directional grain-size heterogeneity, and whether either structure confers a consistent fixed-window depletion advantage.

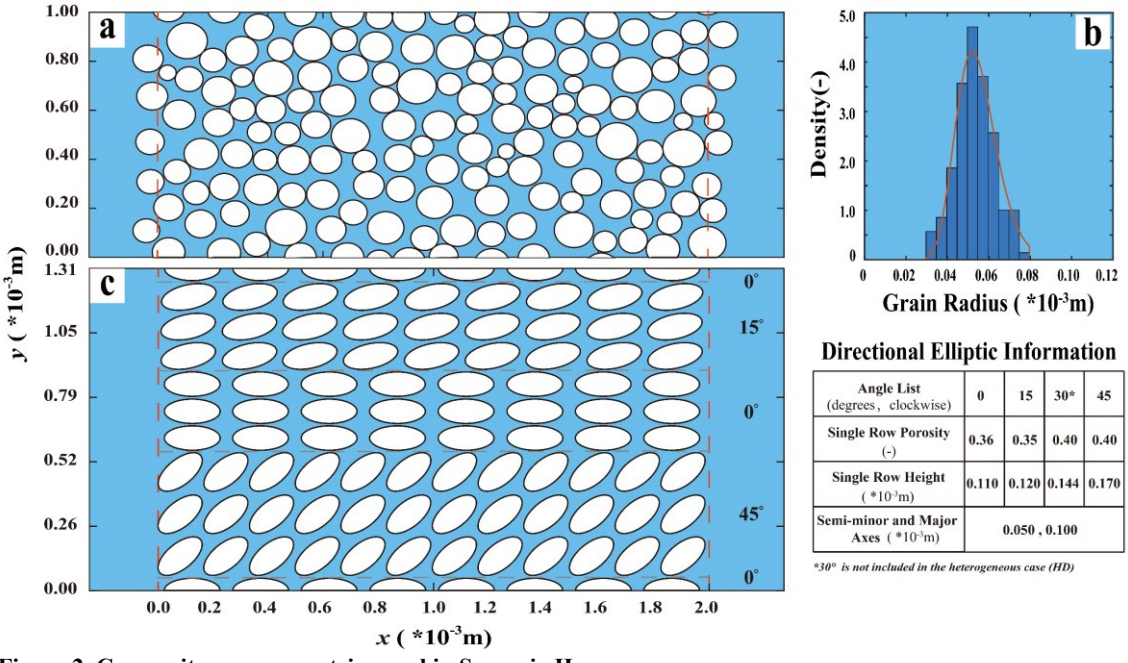

Figure 2. Composite pore geometries used in Scenario II.

(a) Non-directional (ND) geometry generated from a truncated lognormal grain-size distribution; (b) corresponding grain-size distribution following Yang et al. (2022), and (c) heterogeneous directional (HD) geometry constructed by combining subdomains with different ellipse orientations. The uniformly oriented SROE geometries used in Scenario I are not shown because only the packing orientation varies among those cases.

2.2.2 Simulation scenarios and case definition

Two simulation scenarios were designed to separate orientation-associated structural effects from those associated with composite pore architecture. Scenario I comprises four uniformly oriented SROE packings rotated by 0°, 15°, 30°, and 45°, providing a controlled rotation series, whereas Scenario II comprises the two composite geometries, HD and ND, contrasting directional subdomain organization with non-directional grain-size heterogeneity. Within each structural scenario, the simulation matrix was organized around two controlled comparison axes: interfacial-charge parameterization and initial background electrolyte concentration, C_b.

The first comparison evaluated the EDL (DT) and ETL (TT) formulations under matched $C_b = 10$ mM conditions. The second evaluated $C_b = 1$, 10, and 100 mM within the ETL formulation, denoted TO, TT, and TH, respectively. This structure provides a matched-concentration comparison of the two interfacial parameterizations and a separate electrolyte-concentration series within the ETL formulation.

https://doi.org/10.5194/egusphere-2026-4386
Preprint. Discussion started: 4 August 2026

Each simulation label combines the electrochemical group with the pore-structure identifier. For Scenario I, the suffixes 0, 15, 30, and 45 denote the clockwise rotation angles of the SROE packings, whereas for Scenario II, the suffixes HD and ND denote the two composite geometries. For example, TT30 represents the ETL formulation at 10 mM in the 30° SROE packing, whereas TTHD denotes the same electrochemical setting in the heterogeneous directional composite.

The complete simulation matrix comprises 16 Scenario I simulations and 8 Scenario II simulations, giving 24 simulations in total (Table 1). Each simulation differs from the others by only one or two predefined model factors, enabling direct process-based comparisons across structural and electrochemical conditions.

Table 1. Simulation matrix defined by interfacial-charge parameterization, initial background electrolyte concentration, and pore geometry.

Scenario	Geometry	Structure	ETL–1 mM (TO)	ETL–10 mM (TT)	ETL–100 mM (TH)	EDL–10 mM (DT)
Scenario I	Uniformly oriented SROE packing	0°	TO0	TT0	TH0	DT0
		15°	TO15	TT15	TH15	DT15
		30°	TO30	TT30	TH30	DT30
		45°	TO45	TT45	TH45	DT45
Scenario II	Heterogeneous directional composite	HD	TOHD	TTHD	THHD	DTHD
	Non-directional composite	ND	TOND	TTND	THND	DTND

Note: *TO, TT, and TH denote the ETL formulation at C_b = 1, 10, and 100 mM, respectively, whereas DT denotes the EDL formulation at C_b = 10 mM. The suffixes 0, 15, 30, and 45 indicate the clockwise rotation angle of the SROE packing, and HD and ND denote the heterogeneous directional and non-directional composite geometries, respectively. The DT–TT comparison evaluates the two selected interfacial-charge parameterizations under matched 10 mM conditions, whereas the TO–TT–TH sequence evaluates electrolyte-concentration effects within the ETL formulation.*

2.3 Numerical implementation and boundary conditions

2.3.1 Aqueous species and numerical implementation

The aqueous system comprises four ionic species, H^+, OH^-, Na^+, and Cl^-, together with an idealized conservative neutral tracer, denoted Org. Water autoionization is imposed as an instantaneous equilibrium constraint, $C_{H^+}C_{OH^-} = K_w$. Activity coefficients are set to unity, and aqueous activities are therefore approximated by molar concentrations. This ideal-solution approximation is applied consistently across all simulations to enable controlled comparisons among interfacial parameterizations, background electrolyte concentrations, and pore geometries. At C_b = 100 mM, non-ideal activity effects may influence the absolute interfacial potentials and transport rates. The 100 mM cases are therefore used primarily to evaluate concentration-dependent trends within the ETL formulation. The implementation of water autoionization at the electrode boundaries is described in Sect. S2.

Org represents a conservative dissolved neutral tracer transported by molecular diffusion and electroosmotic advection, without electromigration, sorption, degradation, or aqueous reaction. It is used to isolate advective–diffusive displacement under the tested electroosmotic conditions. The molecular diffusivity of Org was fixed at 2.03×10^{-9} $m^2 \cdot s^{-1}$, equal to that of Cl^-, and was applied consistently across all simulations.

https://doi.org/10.5194/egusphere-2026-4386
Preprint. Discussion started: 4 August 2026

The computational domains were discretized using geometry-adaptive unstructured meshes. Depending on the pore geometry, the meshes contained approximately 1×10^5–2×10^5 elements and 3×10^6–6×10^6 degrees of freedom. The same meshing strategy and boundary-refinement criteria were applied across cases to maintain a consistent numerical representation of grain surfaces and concentration gradients.

All simulations were performed for 30 min using COMSOL Multiphysics 5.6. A common simulation window was adopted to compare early displacement, intermediate redistribution, and late-time tracer persistence across all cases. For slowly progressing cases, threshold-based metrics that were not reached within this period were treated as right-censored. Representative ETL cases were recalculated using relative nonlinear-solver tolerances of 5×10^{-3}, 10^{-3}, and 10^{-4}. Across the tested tolerance range, changes in ζ, electroosmotic mobility, and the reported plume descriptors were negligible relative to the contrasts among cases, indicating that the reported comparisons were insensitive to nonlinear-solver tolerance. Spatial- and temporal-discretization sensitivity was additionally assessed for the representative TT30 case. Across the principal transport metrics, differences between the production mesh M2 and the fine-reference mesh M3 were at most 0.421%, while reducing the production maximum time step on M2 to one-quarter changed the metrics by at most 1.445%. Further details are provided in Sect. S5 and Table S7.

Table 2. Physical properties and aqueous diffusion coefficients used in the pore-scale simulations.

Parameter	Symbol	Value	Source
Temperature	T	298.15 K	This study
Fluid density	ρ	1000 kg·m^{-3}	
Dynamic viscosity	μ	1.01×10^{-3} Pa·s	
Relative permittivity of the aqueous phase	ε_r	80	
Molecular diffusivity of OH^-	D_{OH^-}	5.27×10^{-9} m^2·s^{-1}	Lide (2002)
Molecular diffusivity of H^+	D_{H^+}	9.31×10^{-9} m^2·s^{-1}	
Molecular diffusivity of Na^+	D_{Na^+}	1.33×10^{-9} m^2·s^{-1}	
Molecular diffusivity of Cl^-	D_{Cl^-}	2.03×10^{-9} m^2·s^{-1}	
Molecular diffusivity of Org	D_{Org}	2.03×10^{-9} m^2·s^{-1}	

Note: *Org denotes the conservative neutral tracer used to isolate advective–diffusive transport. Its diffusivity was set equal to that of* Cl^-.

2.3.2 Boundary and initial conditions

The anode and cathode are located at the left and right lateral boundaries, respectively. Equal hydraulic pressures are imposed at the two lateral boundaries, such that no external pressure gradient acts across the domain. A potential difference of 0.25 V was imposed over the full 2.5 mm electrode-to-electrode computational length, comprising the 2.0 mm porous test section and two 0.25 mm buffer zones, corresponding to a nominal electric-field strength of 100 V m^{-1} (1 V cm^{-1}). The top and bottom boundaries are periodic for fluid flow, aqueous-species transport, and electric potential.

At grain surfaces, the normal fluid velocity is zero, and the tangential velocity is prescribed by the Helmholtz–Smoluchowski slip condition in Eq. (3). All aqueous species satisfy a zero-normal-flux condition at the solid boundaries. The interfacial-

https://doi.org/10.5194/egusphere-2026-4386
Preprint. Discussion started: 4 August 2026

charge parameterizations update the local zeta potential but do not introduce explicit surface-reaction source or sink terms into the aqueous species balances, as described in Sect. 2.1.1.

The porewater is initially uniform at pH 7 and at the prescribed background electrolyte concentration, C_b. The initial concentrations of Na^+ and Cl^- are both set to C_b, while the initial H^+ and OH^- concentrations are consistent with water autoionization at pH 7. Time-dependent acid and base boundary conditions were applied at the anode and cathode, respectively, using the electrolysis-driven electrode-chamber mass balances described in Sect. S2 and Table S2.

Org was initialized at 1 mol·m^{-3} within the central porous test section, hereafter termed the contaminated medium zone (CMZ), and at zero concentration in the anode and cathode buffer zones. Both lateral electrode boundaries are assigned $C_{\mathrm{Org}} = 0$, providing Dirichlet sink conditions for tracer reaching the domain boundaries. This condition represents immediate removal of tracer entering the idealized electrode chambers. Accordingly, the CMZ-based metrics quantify tracer depletion from the initially contaminated region, irrespective of whether the displaced tracer remains in the buffer zones or leaves through a lateral boundary.

2.4 Evaluation metrics and plume analysis

Model outputs were evaluated using complementary temporal and spatial diagnostics. Boundary- and zone-averaged quantities were used to characterize the temporal evolution of aqueous chemistry, interfacial electrokinetic response, and porewater flow. Metrics calculated for the contaminated medium zone (CMZ) quantify fixed-time depletion and late-time persistence, whereas case-specific relative-progress descriptors compare plume organization at matched fractions of each case's 30 min CMZ depletion. Together, these diagnostics distinguish differences in transport magnitude and timescale from differences in spatial plume organization.

2.4.1 Boundary- and zone-averaged diagnostics

For a generic field variable $X(\boldsymbol{x}, t)$, averages over an external electrode boundary, the internal grain–fluid boundary, and a fluid-filled model subdomain are defined by Eqs. (7)–(9), respectively.

$$\langle X \rangle_{\Gamma_{eb}}(t) = \frac{1}{|\Gamma_{eb}|} \int_{\Gamma_{eb}} X(\boldsymbol{x}, t) d\Gamma, \quad \Gamma_{eb} \in \{\Gamma_A, \Gamma_C\}, \tag{7}$$

$$\langle X \rangle_{\Gamma_{ib}}(t) = \frac{1}{|\Gamma_{ib}|} \int_{\Gamma_{ib}} X(\boldsymbol{x}, t) d\Gamma, \tag{8}$$

$$\langle X \rangle_{\Omega_k}(t) = \frac{1}{|\Omega_k|} \int_{\Omega_k} X(\boldsymbol{x}, t) d\Omega, \quad k \in \{\mathrm{CMZ}, \mathrm{ABZ}, \mathrm{CBZ}\}. \tag{9}$$

Here, Γ_A and Γ_C denote the external anode and cathode boundaries, Γ_{ib} denotes the internal grain–fluid boundary and Ω_{ABZ}, Ω_{CMZ}, and Ω_{CBZ} denote the fluid-filled portions of the anode buffer zone, contaminated medium zone, and cathode buffer zone, respectively. The quantities $|\Gamma|$ and $|\Omega|$ denote boundary length and fluid-domain area in the two-dimensional model.

https://doi.org/10.5194/egusphere-2026-4386
Preprint. Discussion started: 4 August 2026

External-boundary averages were calculated for the concentration of Na^+, Cl^-, and H^+. Under the ideal-activity assumption, pH was calculated as $pH = -\log_{10}(C_{H^+})$, with C_{H^+} expressed in $mol \cdot L^{-1}$. Internal-boundary diagnostics included the zeta potential, electroosmotic mobility, gradient-aligned and gradient-transverse components of electroosmotic slip velocity, and the corresponding components of the tangential electric field. Zone-averaged quantities included Org concentration, pH, and porewater speed, $U(\boldsymbol{x}, t) = ||\mathbf{u}(\boldsymbol{x}, t)||$. Although no externally imposed pressure gradient was applied, local pressure gradients developed within the pore space to satisfy incompressibility and the geometric constraints imposed by the grain surfaces.

2.4.2 CMZ depletion and late-time persistence metrics

Because Org was initially present only in the CMZ, tracer depletion from the initially contaminated region was quantified using the normalized CMZ-averaged concentration defined in Eq. (10). Three complementary metrics were derived from this quantity. The 30 min CMZ depletion fraction in Eq. (11) measures the fraction of the initial normalized concentration depleted from the CMZ by t = 30 min. The time to 90 % CMZ depletion in Eq. (12) is defined as the first time at which the normalized CMZ concentration decreases to 0.10. Late-time persistence is quantified using the dimensionless CMZ tailing index in Eq. (13), defined as the mean normalized CMZ concentration over the 15–30 min interval. Larger tailing index values therefore indicate stronger persistence of tracer within the initially contaminated region.

$$f_{\mathrm{CMZ}}(t) = \frac{\langle c_{\mathrm{Org}} \rangle_{\Omega_{\mathrm{CMZ}}}(t)}{\langle c_{\mathrm{Org}} \rangle_{\Omega_{\mathrm{CMZ}}}(0)}, \tag{10}$$

$$\eta_{30,\mathrm{CMZ}} = 1 - f_{\mathrm{CMZ}}(30\ \mathrm{min}), \tag{11}$$

$$t_{90,\mathrm{CMZ}} = \min\{ t : f_{\mathrm{CMZ}}(t) \leq 0.10 \}, \tag{12}$$

$$TI_{\mathrm{CMZ}} = \frac{1}{15\ \mathrm{min}} \int_{15\ \mathrm{min}}^{30\ \mathrm{min}} f_{\mathrm{CMZ}}(t) dt\ . \tag{13}$$

When 90 % CMZ depletion was not reached within the 30 min simulation window, the corresponding threshold time was treated as right-censored and reported as > 30 min. Time integrals were evaluated from the discrete model outputs using numerical quadrature.

2.4.3 Relative-progress plume characterization and moment descriptors

Comparisons at a fixed physical time combine differences in transport rate with differences in plume morphology. To distinguish these effects, Org concentration fields were additionally evaluated at case-specific relative CMZ-depletion progress levels (de Barros et al., 2013; Fiori, 2014). Relative progress was quantified using Eq. (14).

$$P(t) = \frac{f_{\mathrm{CMZ}}(0) - f_{\mathrm{CMZ}}(t)}{f_{\mathrm{CMZ}}(0) - f_{\mathrm{CMZ}}(t_{end})}, \quad t_{end} = 30\ \mathrm{min}\ . \tag{14}$$

https://doi.org/10.5194/egusphere-2026-4386
Preprint. Discussion started: 4 August 2026

Because the normalized CMZ concentration equals 1 at $t = 0$, this quantity represents the fraction of each case's own 30 min CMZ depletion achieved by time t. Equal progress values therefore do not indicate equal absolute CMZ concentrations, equal tracer masses, or equal whole-domain displacement across cases. First-attainment times therefore describe how rapidly each case approached its own 30 min depletion endpoint and were not used as standalone measures of absolute or fixed-window depletion performance.

Small non-monotonic variations in the discrete progress series $P(t)$ were handled by applying the cumulative-maximum transformation defined in Sect. S3.1. Three target progress levels, p_s = 0.25, 0.60, and 1.00, were selected. For each target, the stage time, t_{p_s}, was defined as the first time at which the monotonized progress series reached that level and was determined by linear interpolation between the two adjacent saved outputs. The 0.25 and 0.60 levels represent early and intermediate fractions of each case's within-window CMZ depletion, respectively. The 1.00 level represents the first attainment of the CMZ depletion observed at t = 30 min. It may therefore occur before the final output time if the CMZ concentration subsequently exhibits a small rebound. Concentration fields were extracted from the saved output nearest to the interpolated stage time; the model-output interval was 0.05 min. Further details are provided in Sect. S3.1.

At each stage-aligned time, position and shape were characterized over a common fluid-filled analysis domain using the zeroth concentration moment M_0, plume-centroid coordinates $(\tilde{v}_x, \tilde{v}_y)$, concentration-weighted covariance tensor $\mathbf{COV}$, principal-axis orientation θ, and anisotropy ratio $R_P = \lambda_1/\lambda_2$, $\lambda_1 \geq \lambda_2$ (Boso et al., 2013; de Barros et al., 2016). The centroid describes plume position, θ describes the dominant plume orientation, and R_P quantifies elongation along the major relative to the minor principal axis. Full definitions and computational details are provided in Sect. S3.2.

Relative-progress alignment was used only to compare plume morphology and spatial organization at normalized stages. In Scenario I, it was used to identify rotation-associated plume reorientation independently of transport-rate differences; in Scenario II, it was used to compare directional plume advancement and organization between HD and ND at case-specific matched stages. Absolute transport rates and fixed-window depletion remained quantified using the CMZ depletion fraction, threshold time, and tailing index.

2.4.4 Plume-aligned ridge analysis for Scenario II

For the composite geometries in Scenario II, an additional plume-aligned analysis was used to identify resolved multipeak concentration patterns (Jiménez-Martínez et al., 2017; de Dreuzy et al., 2012; Sole-Mari et al., 2020; Hyman, 2020; Palodhi and Mishra, 2025). The analysis was restricted to Scenario II because the composite structures were more likely than the uniformly oriented packings to produce projected profiles with multiple local maxima. At each selected progress level, the concentration field was transformed into coordinates centred on the plume centroid and aligned with its major principal axis. The field was then resampled within an adaptive window, and a one-dimensional profile was obtained by maximum projection across the transverse coordinate. The coordinate transformation, resampling procedure, and profile construction are described in Sect. S3.3–S3.5.

https://doi.org/10.5194/egusphere-2026-4386
Preprint. Discussion started: 4 August 2026

After normalization and smoothing, local maxima were identified using fixed criteria for peak height, prominence, and minimum separation. The number of resolved concentration ridges is denoted N_{peaks}. When $N_{\mathrm{peaks}} \geq 2$, the median adjacent-peak distance PS, and its interquartile range PS_{IQR}, were reported as measures of characteristic ridge spacing and spacing variability, respectively. When $N_{\mathrm{peaks}} < 2$, these quantities were undefined, indicating a unimodal or insufficiently resolved projected profile rather than numerical failure. Because the detected maxima represent concentration ridges in a projected plume profile rather than individual pores or pore throats, these metrics were used only as supplementary spatial descriptors and not to rank overall displacement performance or infer pore-size distributions. The complete detection procedure is provided in Sect. S3.6.

3 Results

3.1 Cross-case CMZ depletion and persistence

Tracer depletion from the initially contaminated region was evaluated using the 30 min CMZ depletion fraction, $\eta_{30,\mathrm{CMZ}}$, the time to 90 % CMZ depletion, $t_{90,\mathrm{CMZ}}$, and the window-based CMZ tailing index, TI_{CMZ}, calculated over 15–30 min. Case-specific values are reported in Table S3, whereas Table 3 summarizes the variation of these metrics across the tested pore geometries.

Table 3. Descriptive summaries of CMZ depletion and persistence metrics across the tested pore geometries.

Series	Structural subset	$\eta_{30,\mathrm{CMZ}}$	$t_{90,\mathrm{CMZ}}$(min)	TI_{CMZ}
TO	TO0–TO45	0.961 ± 0.014	7.89 ± 1.57	0.040 ± 0.015
	TOHD–TOND	0.967 ± 0.016	8.88 ± 1.17	0.033 ± 0.016
	TO0–TOND	0.963 ± 0.013	8.22 ± 1.42	0.037 ± 0.014
TT	TT0–TT45	0.915 ± 0.019	19.22 ± 7.03	0.095 ± 0.027
	TTHD–TTND	0.924 ± 0.018	18.74 ± 0.60	0.093 ± 0.004
	TT0–TTND	0.918 ± 0.018	19.06 ± 5.68	0.094 ± 0.021
TH	TH0–TH45	0.596 ± 0.048	> 30.00 (4/4 censored)	0.474 ± 0.043
	THHD–THND	0.647 ± 0.088	> 30.00 (2/2 censored)	0.448 ± 0.086
	TH0–THND	0.613 ± 0.060	> 30.00 (6/6 censored)	0.465 ± 0.053
DT	DT0–DT45	0.998 ± 0.001	2.76 ± 0.41	0.002 ± 0.001
	DTHD–DTND	0.998 ± 0.001	3.22 ± 0.52	0.002 ± 0.001
	DT0–DTND	0.998 ± 0.001	2.92 ± 0.46	0.002 ± 0.001

***Note**: Case-specific values are provided in Table S3. Values are reported as the mean ± standard deviation across the indicated deterministic pore geometries. For groups containing right-censored $t_{90,CMZ}$ values, censored observations were represented at the 30 min simulation limit. The resulting summaries are therefore descriptive lower bounds and should not be interpreted as estimates of the uncensored threshold-time distribution.*

Clear group-level contrasts were observed in all three CMZ metrics (Fig. 3). Under the matched 10 mM background electrolyte condition, the EDL group (DT) showed a mean 30 min depletion fraction of 0.998, compared with 0.918 for the ETL group (TT). The corresponding mean tailing indices were 0.002 and 0.094. All DT cases reached 90 % CMZ depletion within 2.44–3.59 min, whereas the TT threshold times ranged from 13.89 to 19.16 min among the cases that reached the threshold; TT0 remained right-censored at 30 min.

https://doi.org/10.5194/egusphere-2026-4386
Preprint. Discussion started: 4 August 2026

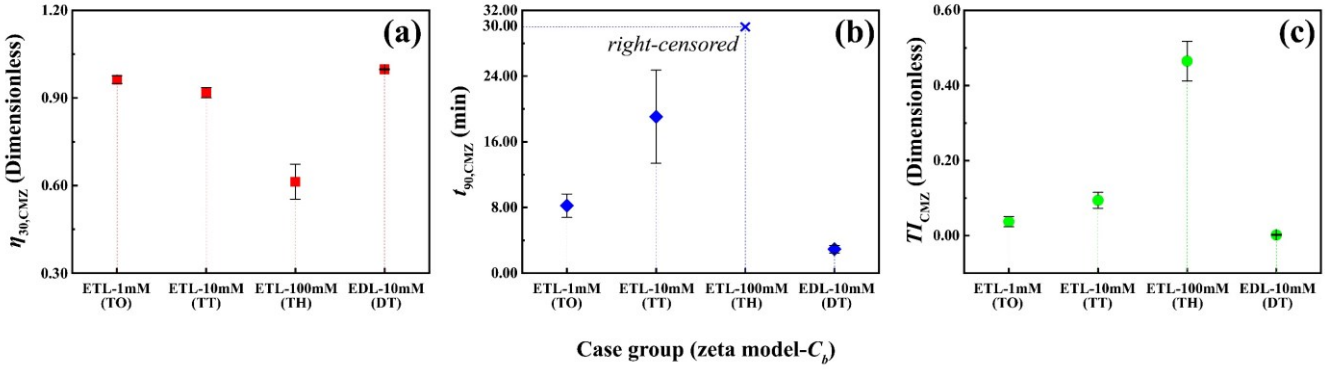

Figure 3. CMZ depletion and persistence metrics across the four interfacial electrochemical groups.

(a) CMZ depletion fraction after 30 min, $\eta_{30,CMZ}$; (b) time to 90 % CMZ depletion, $t_{90,CMZ}$; and (c) CMZ tailing index, TI_{CMZ}, averaged over 15–30 min. TO, TT, and TH denote the ETL formulation at C_b = 1, 10, and 100 mM, respectively, whereas DT denotes the EDL formulation at C_b = 10 mM. Symbols show descriptive means across the six tested pore geometries, and error bars show the corresponding standard deviations among those geometries. Right-censored $t_{90,CMZ}$ values are displayed at the 30 min observation limit using distinct symbols.

Within the ETL formulation, increasing the background electrolyte concentration progressively reduced CMZ depletion and increased late-time persistence. The mean 30 min depletion fraction decreased from 0.963 for TO to 0.918 for TT and 0.613 for TH, while the mean tailing index increased from 0.037 to 0.094 and 0.465. All TO cases reached 90 % CMZ depletion within 6.68–10.19 min. In contrast, none of the TH cases reached this threshold within the 30 min simulation window.

Within-group differences among pore geometries remained detectable, although their magnitude depended on both the electrochemical setting and the metric considered (Table S3). The TT group showed the widest structure-associated range in $t_{90,CMZ}$, extending from 13.89 min to > 30 min, whereas the DT cases differed only slightly in depletion and tailing. Because all TH cases were right-censored for $t_{90,CMZ}$, their structural differences were expressed more clearly by the fixed-time metrics: the 30 min depletion fraction ranged from 0.553 to 0.710, and the tailing index ranged from 0.387 to 0.515.

Across the complete case matrix, the three CMZ metrics showed a consistent group-level ordering: DT exhibited the greatest 30 min depletion and weakest late-time persistence, followed by TO and TT, whereas TH showed the lowest depletion and strongest persistence. These between-group contrasts were generally larger than the differences among pore geometries within the same group. Sections 3.2 and 3.3 therefore examine how pore structure modifies velocity partitioning and plume organization within these broader electrochemical transport regimes.

3.2 Scenario I: Orientation-associated structural effects in SROE packings

3.2.1 Zone-averaged evolution of Org, pH, and porewater velocity

Figure 4 shows the temporal evolution of zone-averaged Org concentration and pH in the anode buffer zone (ABZ), contaminated medium zone (CMZ), and cathode buffer zone (CBZ). The corresponding zone-averaged porewater speeds are

https://doi.org/10.5194/egusphere-2026-4386
Preprint. Discussion started: 4 August 2026

shown in Fig. S1a–c. Across all electrochemical groups, Org was progressively depleted from the CMZ and redistributed into the adjacent buffer zones, but the transport timescales differed markedly among DT, TO, TT, and TH.

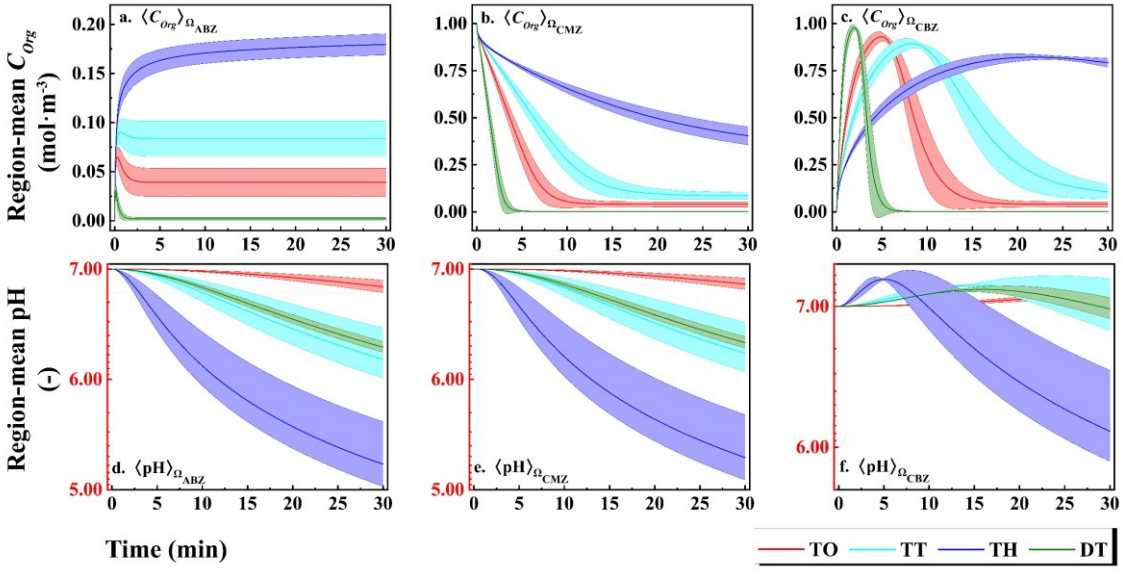

Figure 4. Temporal evolution of zone-averaged Org concentration and pH in the four SROE geometries.

Panels (a–c) show Org concentration in the anode buffer zone (ABZ), contaminated medium zone (CMZ), and cathode buffer zone (CBZ), respectively; panels (d–f) show the corresponding zone-averaged pH. Solid curves represent descriptive means across the four packing orientations within each electrochemical group, and shaded bands indicate ±1 standard deviation among the four orientations. TO, TT, and TH denote the ETL formulation at C_b = 1, 10, and 100 mM, respectively, whereas DT denotes the EDL formulation at C_b = 10 mM.

CMZ concentration decreased most rapidly in the DT cases, followed by TO and TT, whereas TH retained the highest concentrations throughout the 30 min simulation period. This ordering is consistent with the CMZ metrics reported in Sect. 3.1. The spread among the four SROE orientations was most evident for TT and TH and remained comparatively small for DT after the initial displacement period. In the buffer zones, the faster DT and TO cases generally showed earlier tracer accumulation and subsequent decline, whereas TT and TH exhibited later redistribution and greater late-time persistence. Orientation-associated differences were most visible during the rising and declining portions of the CBZ concentration curves. Electrolysis also produced distinct pH responses among the electrochemical groups. The ABZ and CMZ became progressively more acidic, with the largest zone-averaged pH decrease occurring in TH and intermediate changes in TT. In the CBZ, several cases showed an initial alkaline excursion followed by stabilization or a later decrease. Both the magnitude and timing of these changes varied among the SROE orientations.

Zone-averaged porewater speed followed the group ordering DT > TO > TT > TH throughout most of the simulation window (Fig. S1a–c). Within each group, the spread among the four SROE geometries was smaller than the separation among electrochemical groups, although persistent orientation-associated differences remained visible in all three zones.

https://doi.org/10.5194/egusphere-2026-4386
Preprint. Discussion started: 4 August 2026

3.2.2 Internal-boundary electrokinetic response

Figure 5 summarizes electrokinetic quantities averaged over the internal grain–fluid boundaries within the CMZ. The boundary-averaged zeta potential remained negative in all cases, with its magnitude following the ordering DT > TO > TT > TH. The DT cases also showed the strongest temporal change, becoming progressively less negative, whereas the ETL groups varied less over the 30 min period. Electroosmotic mobility followed the same group ordering and temporal pattern. Within each electrochemical group, differences among the four SROE geometries were substantially smaller than the separation among group-averaged responses.

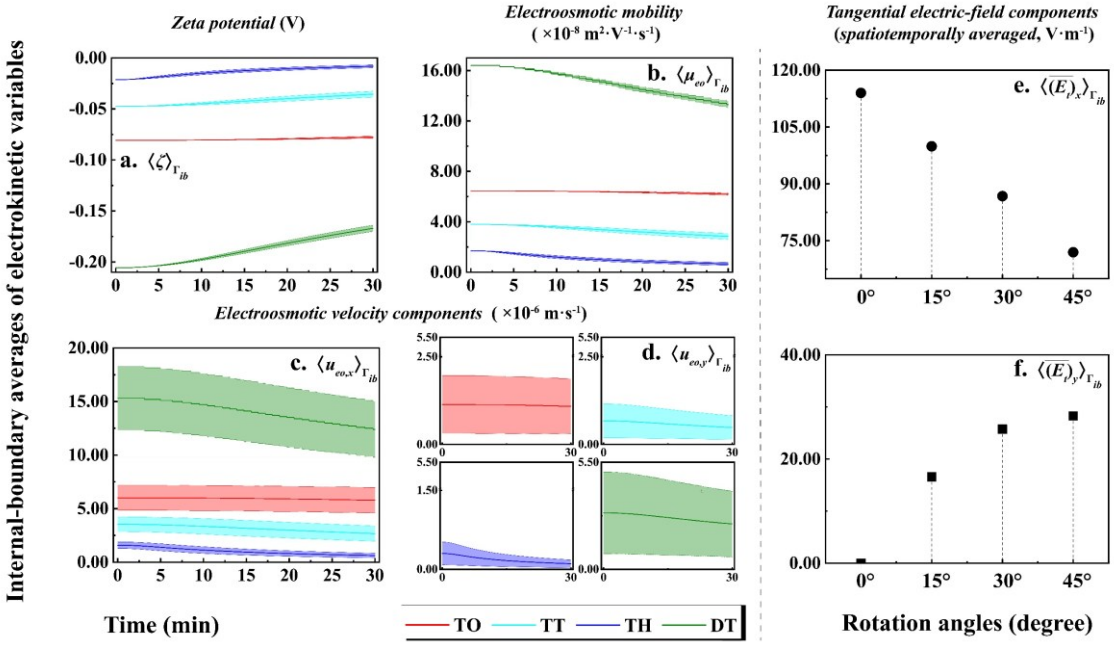

Figure 5. Internal-boundary-averaged electrokinetic quantities within the CMZ for the four SROE geometries.

Panels (a) and (b) show the temporal evolution of the boundary-averaged zeta potential, $\langle\zeta\rangle_{\Gamma_{ib,CMZ}}$, and electroosmotic mobility, $\langle\mu_{eo}\rangle_{\Gamma_{ib,CMZ}}$, respectively. Panels (c) and (d) show the corresponding gradient-aligned and gradient-transverse electroosmotic velocity components, $\langle u_{eo,x}\rangle_{\Gamma_{ib,CMZ}}$ and $\langle u_{eo,y}\rangle_{\Gamma_{ib,CMZ}}$. Panels (e) and (f) show the spatiotemporally averaged gradient-aligned and gradient-transverse components of the tangential electric field as functions of packing-rotation angle. In panels (a–d), solid curves denote descriptive means across the four SROE orientations within each electrochemical group, and shaded bands indicate ± 1 standard deviation among those orientations.

The gradient-aligned component of electroosmotic slip velocity generally followed the ordering DT > TO > TT > TH, whereas the smaller gradient-transverse component was more sensitive to packing orientation. The transverse component was close to zero in the 0° geometries and became increasingly non-zero as the packing was rotated. Consistent directional changes occurred in the tangential electric field: with increasing packing angle, its spatiotemporally averaged gradient-aligned component decreased, while the gradient-transverse component increased from approximately zero (Fig. 5e–f). External electrode-boundary concentrations and pH are reported in Fig. S1d–i; the principal response was progressive acidification at the anode and alkalization at the cathode.

https://doi.org/10.5194/egusphere-2026-4386
Preprint. Discussion started: 4 August 2026

3.2.3 Orientation-associated differences under the TT setting

The TT group was selected for detailed comparison because it showed the widest orientation-associated range in the CMZ depletion metrics among the Scenario I groups for which most cases reached the 90 % threshold. Figure 6 compares the CMZ-averaged Org concentration and porewater speed with the corresponding internal-boundary electroosmotic-slip components in the four TT geometries.

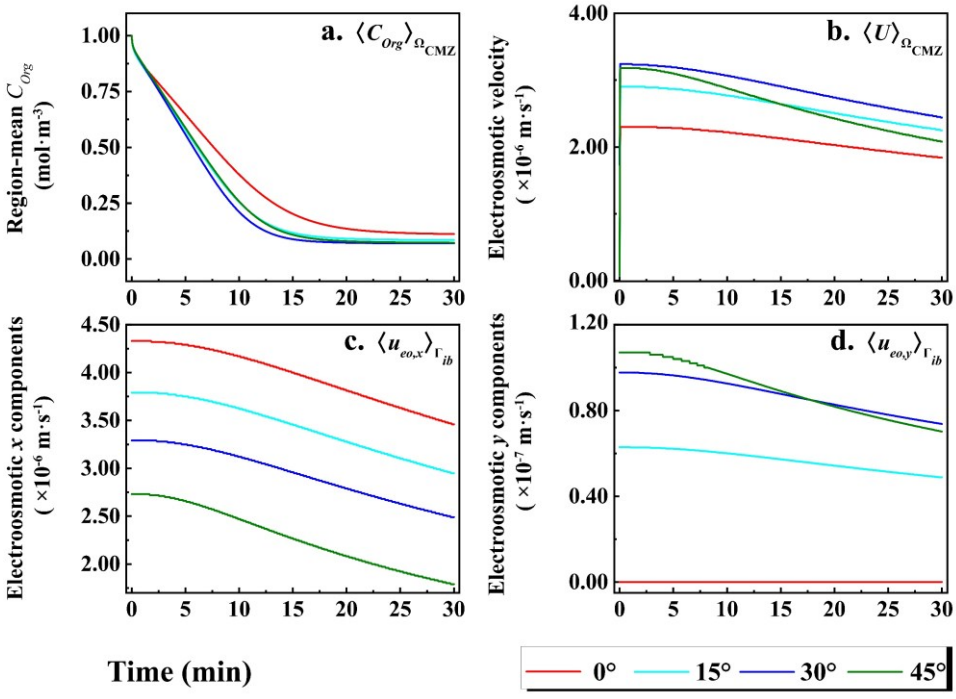

Figure 6. CMZ-averaged Org concentration and porewater speed, together with internal-boundary electroosmotic-slip components, for the four TT SROE geometries.

Panel (a) shows the CMZ-averaged Org concentration, $\langle C_{Org}\rangle_{\Omega_{CMZ}}$; panel (b) shows the CMZ-averaged porewater speed, $\langle U\rangle_{\Omega_{CMZ}}$; and panels (c) and (d) show the internal-boundary-averaged gradient-aligned and gradient-transverse electroosmotic-slip components, $\langle u_{eo,x}\rangle_{\Gamma_{ib}}$ and $\langle u_{eo,y}\rangle_{\Gamma_{ib}}$, respectively. Curves represent the 0°, 15°, 30°, and 45° SROE geometries under the ETL formulation at C_b = 10 mM. Each curve represents one deterministic pore geometry.

The fixed-time CMZ response varied non-monotonically with packing angle (Fig. 6a). After 30 min, the depletion fraction increased from 0.888 in TT0 to 0.915 in TT15 and 0.930 in TT30, before decreasing slightly to 0.927 in TT45 (Table S3). TT30 also showed the lowest tailing index (0.073), whereas TT0 showed the highest value (0.134) and did not reach 90 % depletion within 30 min. Among the remaining cases, the 90 % threshold was reached after 17.21 min in TT15, 13.89 min in TT30, and 15.78 min in TT45.

The CMZ-averaged porewater speed showed a similar non-monotonic response (Fig. 6b), with TT30 maintaining the highest speed and TT0 the lowest over most of the simulation period. By contrast, the internal-boundary electroosmotic-slip

https://doi.org/10.5194/egusphere-2026-4386
Preprint. Discussion started: 4 August 2026

components varied more systematically with orientation: the gradient-aligned component decreased as the packing angle increased, whereas the gradient-transverse component increased from approximately zero at 0°. Together, these orientation-dependent changes were associated with the highest CMZ-averaged porewater speed at the intermediate 30° orientation rather than at either angular endpoint.

Thus, increasing packing angle did not produce a monotonic change in CMZ depletion. Instead, the fixed-time response reflected the combined variation of gradient-aligned and gradient-transverse flow components. The associated plume-scale differences are examined in Sect. 3.2.4.

3.2.4 Stage-aligned plume organization and spatial moments

To distinguish plume morphology from differences in transport timescale, Org concentration fields were compared at relative CMZ-depletion progress levels of 0.25, 0.60, and 1.00. The corresponding first-attainment times are reported in Table S4. As defined in Sect. 2.4.3, equal progress levels represent equal fractions of each case's own 30 min CMZ depletion and not equal absolute residual concentrations.

Stage-attainment times differed substantially among the electrochemical groups. DT reached the early and intermediate progress levels first, whereas TH generally required the longest time to reach 0.60. Within TO, TT, and DT, the 30° geometry reached the 0.60 level earlier than the other SROE geometries, at 3.90, 6.50, and 1.55 min, respectively; within TH, the earliest attainment occurred in TH45 at 9.90 min.

At the intermediate progress level of 0.60, plume migration remained predominantly aligned with the applied electric field, but plume orientation and transverse displacement varied systematically with packing rotation (Fig. 7). The 0° geometries retained an approximately field-aligned major axis and showed little transverse centroid displacement. With increasing packing angle, the plume major axis rotated away from the applied-field direction, accompanied by greater transverse displacement and changes in front shape and trailing-concentration patterns.

https://doi.org/10.5194/egusphere-2026-4386
Preprint. Discussion started: 4 August 2026

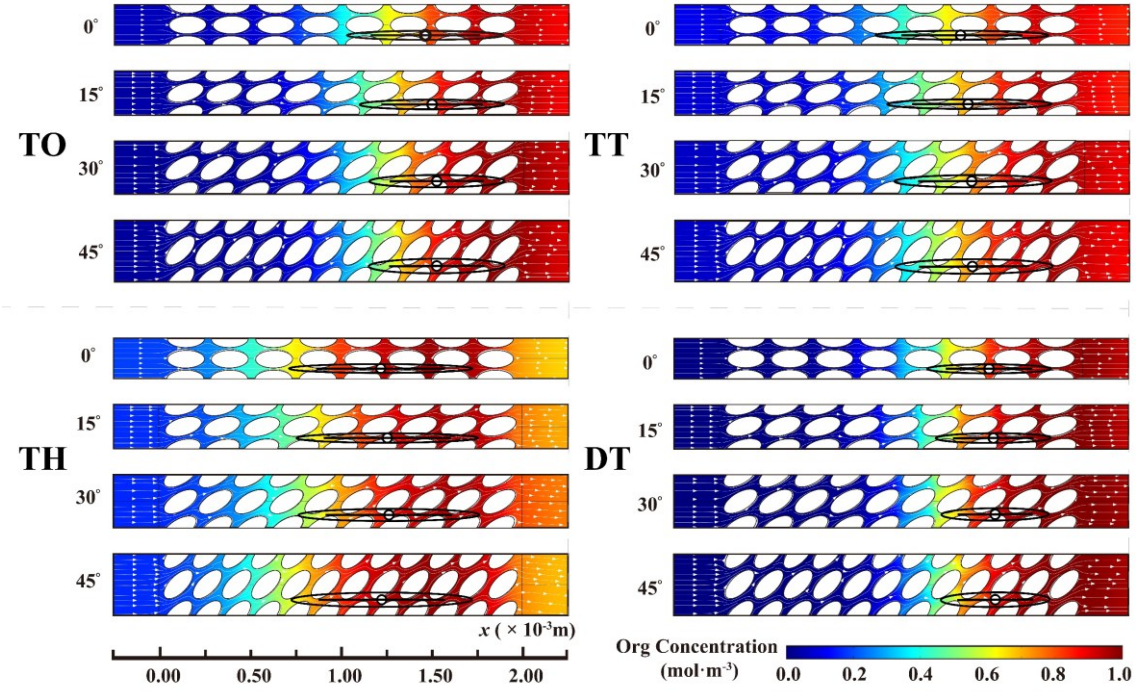

Figure 7. Org concentration fields in the Scenario I SROE geometries at the relative progress level of 0.60.

Columns correspond to packing-rotation angles of 0°, 15°, 30°, and 45°, and rows correspond to the TO, TT, TH, and DT electrochemical groups. White arrows show the local porewater-flow direction. Markers indicate the concentration-weighted plume centroids, and arrows show the major principal-axis orientation obtained from the second spatial moments. All panels use the same concentration colour scale.

The spatial-moment descriptors quantify these differences across the three progress levels (Fig. 8). Principal-axis orientation generally increased with packing angle, particularly at the 0.60 level, indicating systematic plume reorientation with the imposed structural rotation. The anisotropy ratio generally decreased with increasing angle, although both descriptors also evolved with relative progress. The normalized CMZ concentrations shown in Fig. 8 provide the corresponding absolute residual levels but are not independent of the progress-alignment definition.

https://doi.org/10.5194/egusphere-2026-4386
Preprint. Discussion started: 4 August 2026

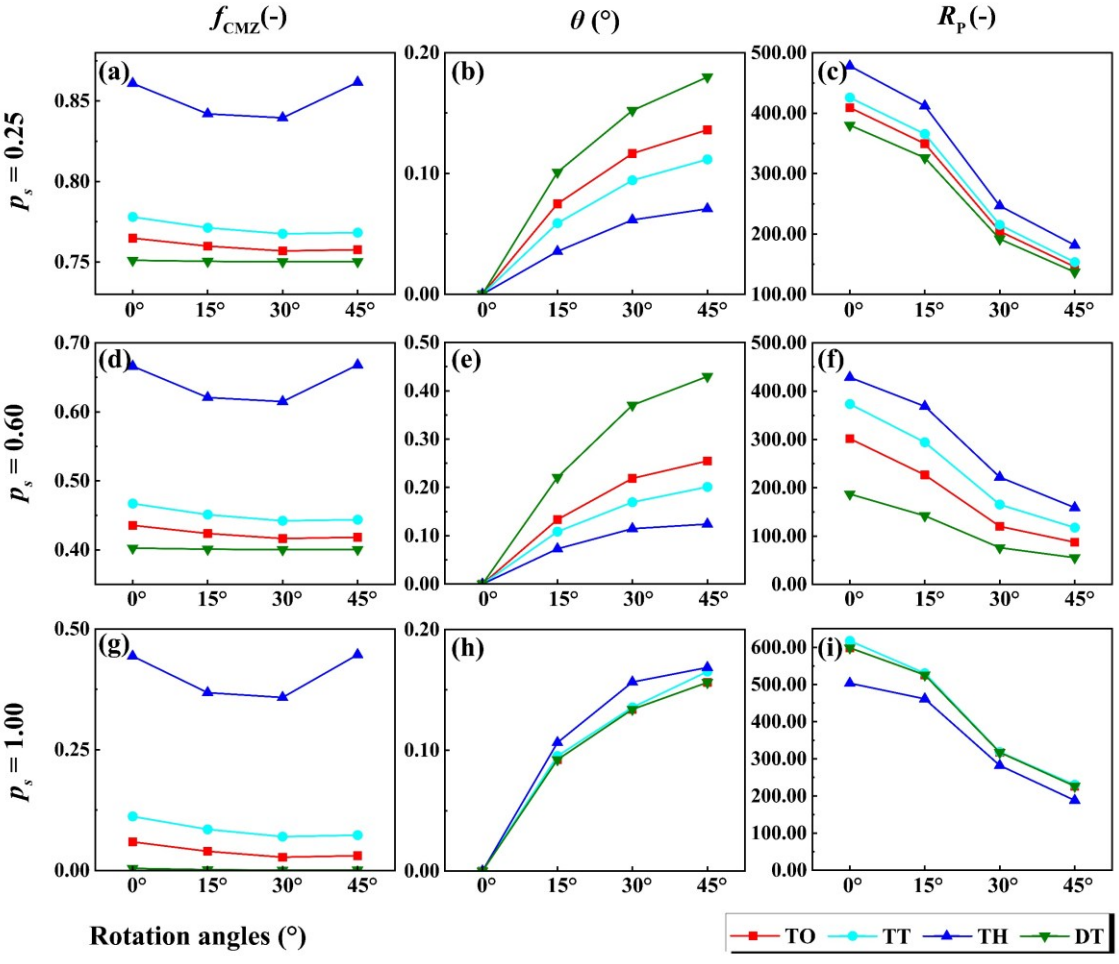

Figure 8. Spatial-moment descriptors for Scenario I at relative progress levels of 0.25, 0.60, and 1.00.

Panels (a, d, g) show the normalized CMZ concentration, f_{CMZ}; panels (b, e, h) show the principal-axis orientation, θ; and panels (c, f, i) show the anisotropy ratio, R_P. Symbols denote the four electrochemical groups, and lines connect the four SROE packing angles within each group. The f_{CMZ} values are shown only to indicate absolute residual concentration and are not independent of the progress-alignment definition.

The gradient-aligned plume centroid advanced as relative progress increased (Fig. 9a). Transverse centroid displacement remained close to zero in the 0° geometries but became non-zero in the rotated packings (Fig. 9b). The largest deviations generally occurred at the intermediate progress level, whereas several cases showed smaller values or changes in sign at 1.00. Transverse displacement was therefore transient and did not necessarily accumulate monotonically over the simulation window.

https://doi.org/10.5194/egusphere-2026-4386
Preprint. Discussion started: 4 August 2026

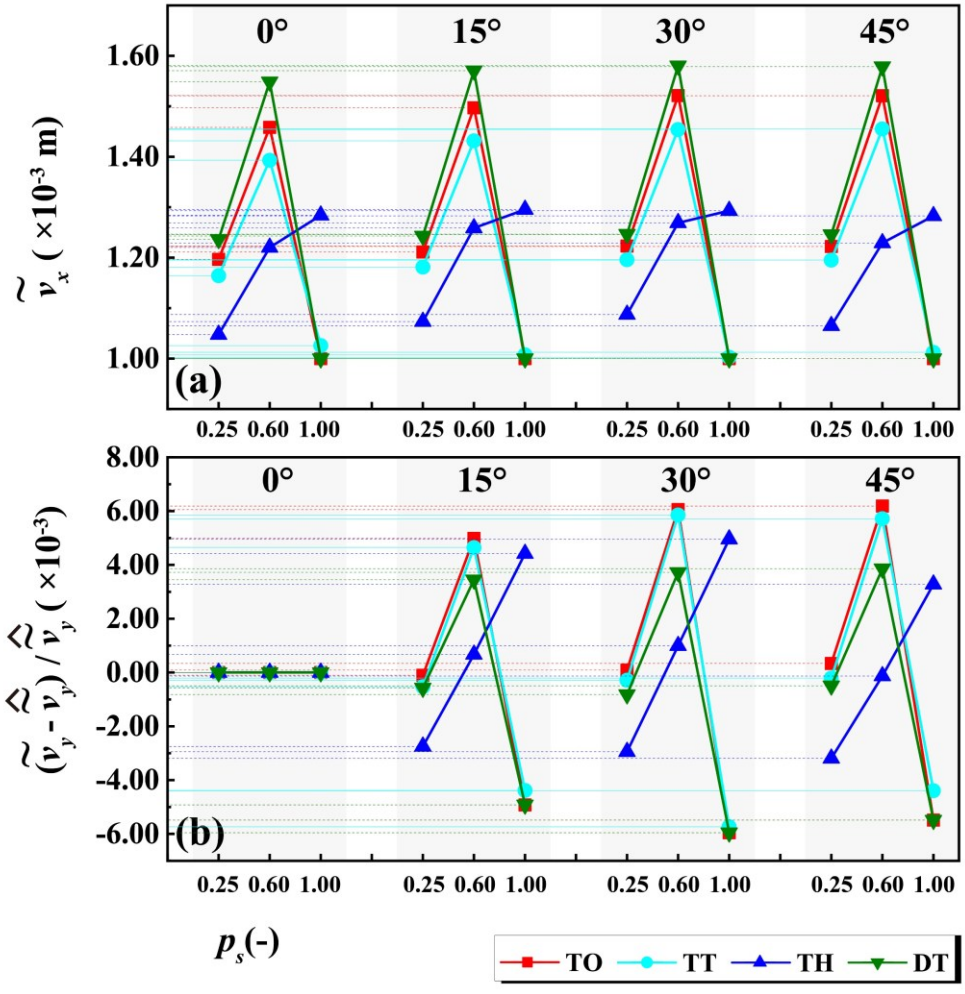

Figure 9. Plume-centroid coordinates for the Scenario I SROE geometries at relative progress levels of 0.25, 0.60, and 1.00.

Panel (a) shows the gradient-aligned centroid coordinate, $\tilde{v}_x$, and panel (b) shows the normalized gradient-transverse centroid displacement, $(\tilde{v}_y - \widehat{\tilde{v}_y})/\widehat{\tilde{v}_y}$, where $\widehat{\tilde{v}_y}$ denotes the average of $\tilde{v}_y$ within the corresponding comparison group. Results are shown for packing-rotation angles of 0°, 15°, 30°, and 45°. Markers denote the TO, TT, TH, and DT electrochemical groups at the three relative progress levels. Dashed lines are included only as visual guides.

Together, the velocity and plume descriptors show that packing rotation primarily modified directional flow partitioning, plume orientation, transient transverse centroid motion, and anisotropy. Electrochemical setting strongly affected the time required to reach the selected progress levels, whereas systematic spatial contrasts remained detectable among orientations within each group. The non-monotonic fixed-time depletion response therefore coexisted with more consistent orientation-associated changes in plume geometry.

https://doi.org/10.5194/egusphere-2026-4386
Preprint. Discussion started: 4 August 2026

3.3 Scenario II: Composite-geometry contrasts between HD and ND

3.3.1 Zone- and boundary-averaged responses in the composite geometries

The zone-averaged Org concentration, pH, and porewater-speed trajectories retained the broad electrochemical-group ordering observed in Scenario I (Figs. S2 and S3). CMZ concentration decreased most rapidly in DT and most slowly in TH, with TO and TT showing intermediate responses. Correspondingly, porewater speed was highest in DT and lowest in TH. Differences in the bulk CMZ response between HD and ND remained detectable within individual electrochemical groups but did not follow a consistent geometry-dependent ordering. The more persistent structural contrast concerned directional flow partitioning and transport timing.

Under TO and TT, ND showed greater CMZ depletion after 30 min than HD. The depletion fractions were 0.978 and 0.956 for TOND and TOHD, respectively, and 0.937 and 0.911 for TTND and TTHD (Table S3). ND also showed slightly lower tailing indices under both settings. However, HD reached the 90 % CMZ depletion threshold earlier: $t_{90,\mathrm{CMZ}}$ was 8.05 min for TOHD compared with 9.71 min for TOND and 18.31 min for TTHD compared with 19.16 min for TTND. Thus, earlier threshold attainment did not necessarily correspond to greater depletion at the end of the simulation window.

A different HD–ND contrast occurred under TH. Neither geometry reached 90 % CMZ depletion within 30 min, but THHD showed a greater 30 min depletion fraction than THND (0.710 compared with 0.585) and a lower tailing index (0.387 compared with 0.508). Under DT, both geometries approached complete CMZ depletion, although DTHD reached the 90 % threshold earlier than DTND, at 2.85 and 3.59 min, respectively. The HD–ND ranking therefore depended on both the electrochemical setting and the metric used to characterize depletion.

The internal-boundary-averaged zeta potential and electroosmotic mobility showed the group ordering DT > TO > TT > TH in magnitude, with only small differences between HD and ND relative to the separation among electrochemical groups (Fig. 10a–b). The gradient-aligned electroosmotic slip velocity followed the same broad ordering but exhibited clearer geometry-dependent differences (Fig. 10c). The strongest directional contrast occurred in the gradient-transverse component: HD maintained a non-zero transverse velocity, whereas the corresponding ND values remained close to zero throughout most of the simulation (Fig. 10d). Consistent differences were observed in the tangential electric field, whose transverse component was non-zero in HD but close to zero when averaged over ND (Fig. 10e).

https://doi.org/10.5194/egusphere-2026-4386
Preprint. Discussion started: 4 August 2026

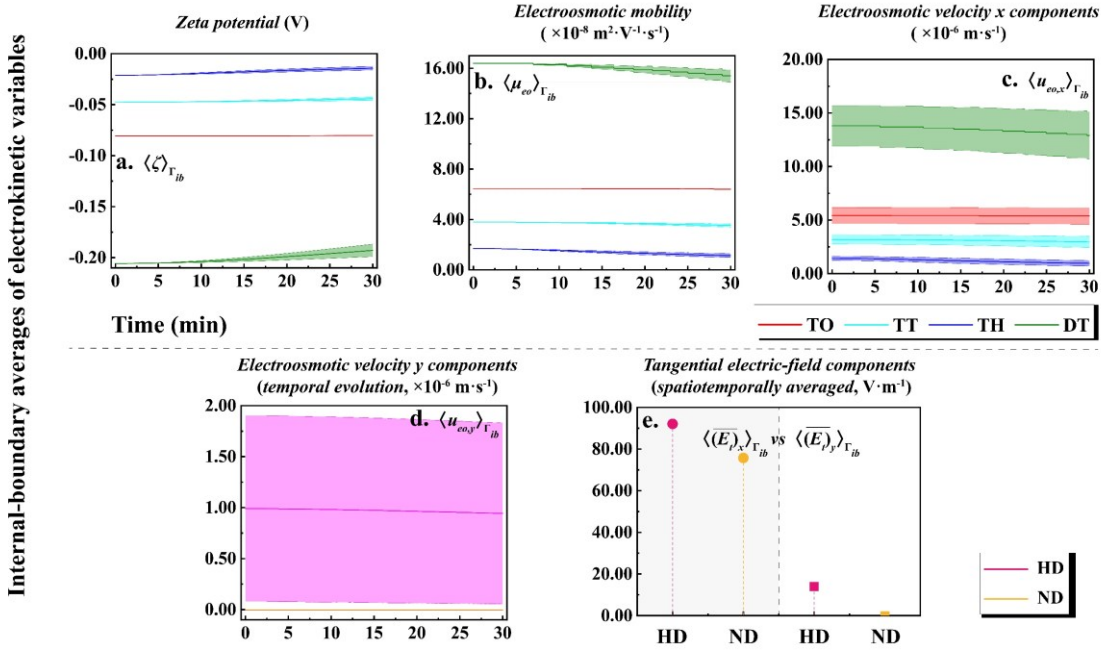

Figure 10. Internal-boundary-averaged electrokinetic quantities for the Scenario II composite geometries.

Panels (a–d) show the temporal evolution of (a) zeta potential, $\langle\zeta\rangle_{\Gamma_{ib}}$; (b) electroosmotic mobility, $\langle\mu_{eo}\rangle_{\Gamma_{ib}}$; (c) gradient-aligned electroosmotic slip velocity, $\langle u_{eo,x}\rangle_{\Gamma_{ib}}$; and (d) gradient-transverse electroosmotic slip velocity, $\langle u_{eo,y}\rangle_{\Gamma_{ib}}$. Colours denote the TO, TT, TH, and DT electrochemical groups. Solid curves show the arithmetic mean of the HD and ND values, and shaded envelopes span the two geometry-specific values. Panel (e) shows the spatiotemporally averaged gradient-aligned and gradient-transverse components of the tangential electric field for HD and ND.

Overall, HD and ND differed little in boundary-averaged zeta potential and electroosmotic mobility but clearly in directional flow organization. HD maintained non-zero domain-averaged transverse electric-field and electroosmotic-slip components, whereas the corresponding ND components remained close to zero after domain averaging. At the CMZ scale, however, the HD–ND ranking remained dependent on the electrochemical setting and evaluation metric. Thus, directional composite organization produced a consistent contrast in domain-scale flow direction without imposing a uniform fixed-window depletion advantage.

3.3.2 Relative-progress plume organization and spatial-moment descriptors

The first-attainment times for the selected relative progress levels are reported in Table S5. In all four electrochemical groups, HD reached the early and intermediate progress levels of 0.25 and 0.60 earlier than ND. At the 1.00 level, HD reached the endpoint-equivalent depletion earlier under TO and DT, whereas both geometries first reached this level at 30 min under TT and TH. These first-attainment times compare how rapidly each geometry approached its own 30 min depletion endpoint; fixed-time HD–ND differences are reported separately in Sect. 3.3.1.

https://doi.org/10.5194/egusphere-2026-4386
Preprint. Discussion started: 4 August 2026

At the intermediate progress level of 0.60, the Org concentration fields showed distinct plume organizations in the two composite geometries (Fig. 11). In HD, plume advancement and orientation varied among subdomains with different prescribed packing directions, producing locally uneven front propagation. In ND, the concentration front was more irregular around the disordered packing region but showed less persistent domain-scale transverse deflection. The HD–ND contrast was therefore expressed through different patterns of local front deformation and domain-scale directional persistence.

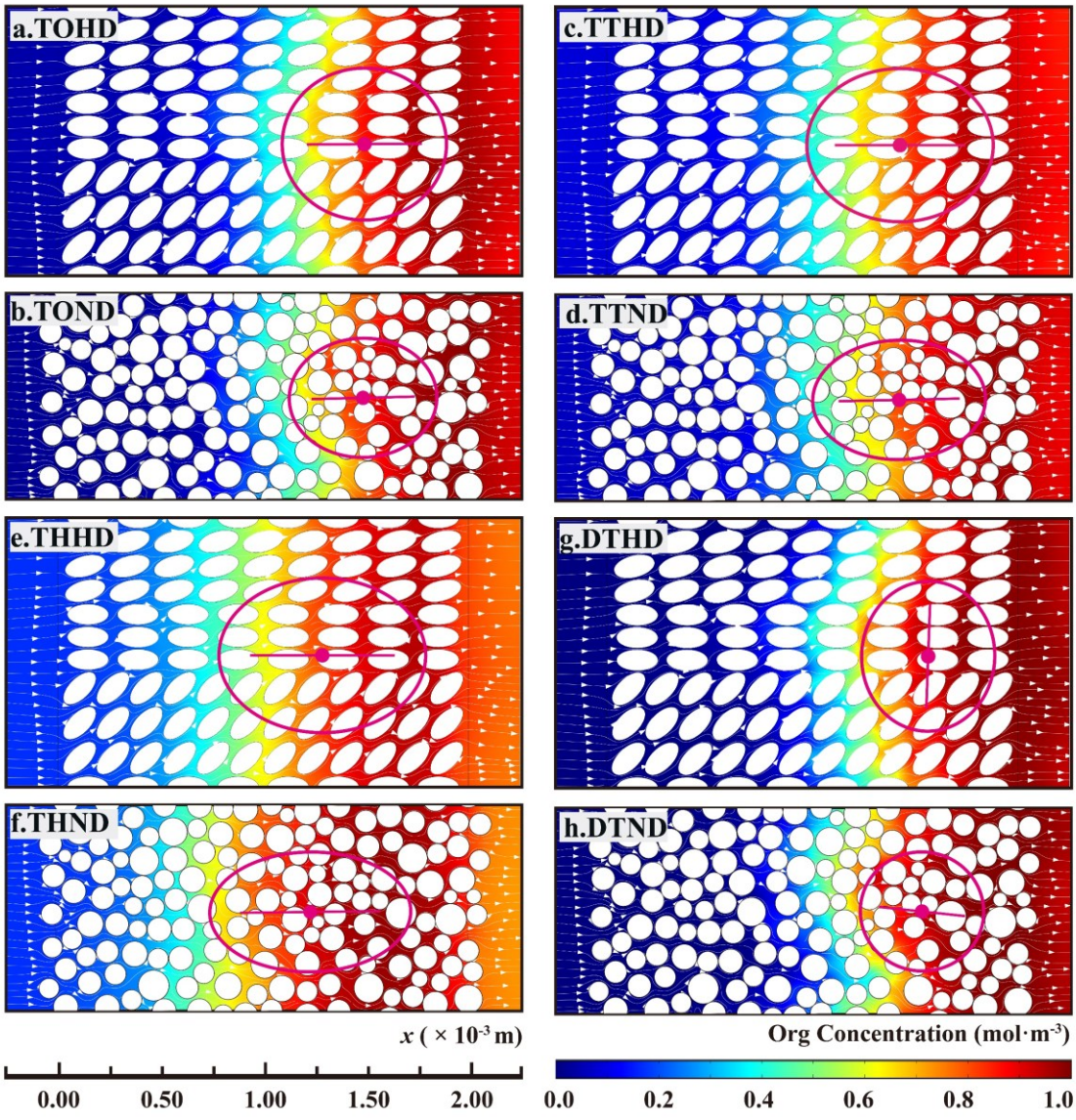

Figure 11. Org concentration fields in the Scenario II composite geometries at the relative progress level of 0.60.

Panels (a, b), (c, d), (e, f), and (g, h) compare HD and ND under the TO, TT, TH, and DT settings, respectively. White arrows indicate porewater-velocity direction; magenta markers, ellipses, and line segments denote plume centroids, second-moment plume shapes, and major principal axes, respectively. All panels use the same concentration colour scale.

https://doi.org/10.5194/egusphere-2026-4386
Preprint. Discussion started: 4 August 2026

At a given relative progress level (Fig. 12), f_{CMZ} retained the corresponding differences in residual CMZ concentration, whereas R_P, θ, and the centroid coordinates described how plume organization evolved within each case. The plume-anisotropy ratio, R_P, varied with both progress level and electrochemical setting, and ND generally showed greater stage-to-stage variation than HD. Unlike the comparatively ordered angle-dependent response in Scenario I, the composite geometries did not exhibit a consistent relationship between R_P and the principal-axis orientation, θ.

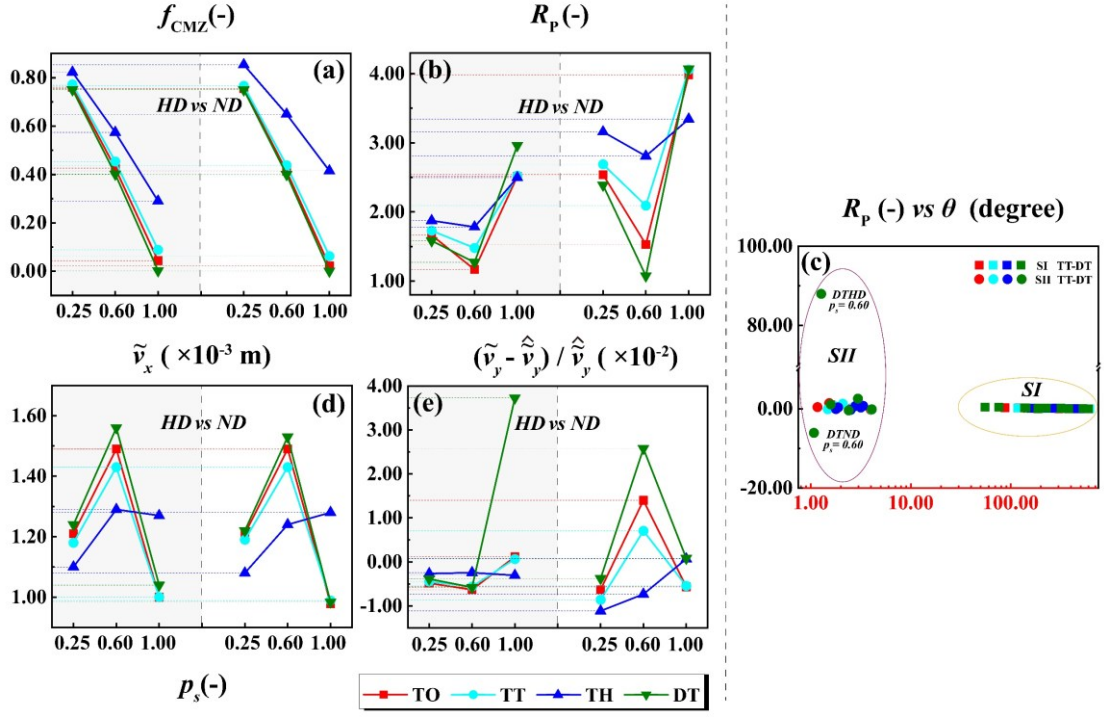

Figure 12. Relative-progress plume descriptors for the Scenario II composite geometries.

Panels show (a) the normalized CMZ concentration, f_{CMZ}; (b) the anisotropy ratio, R_P; (c) the relationship between R_P and the principal-axis orientation, θ, with the Scenario I results included for comparison; (d) the gradient-aligned centroid coordinate, $\tilde{v}_x$; and (e) the normalized gradient-transverse centroid displacement, $(\tilde{v}_y - \widehat{\tilde{v}_y})/\widehat{\tilde{v}_y}$, where $\widehat{\tilde{v}_y}$ denotes the average of $\tilde{v}_y$ within the corresponding comparison group. Results are shown at p_s = 0.25, 0.60, and 1.00 for the HD and ND geometries under the TO, TT, TH, and DT settings. The R_P axis in panel (c) is logarithmic.

The gradient-aligned centroid, $\tilde{v}_x$, was generally farther advanced in HD than in ND at the same relative progress level. By contrast, the normalized gradient-transverse centroid displacement remained small in many cases and showed no consistent HD–ND ordering across electrochemical groups or progress levels, although a clearer late-stage transverse displacement occurred in DTHD. Overall, earlier attainment of case-specific progress levels and greater gradient-aligned centroid advancement were the main consistent HD–ND contrasts, whereas plume anisotropy and transverse centroid displacement showed no uniform geometry ranking.

https://doi.org/10.5194/egusphere-2026-4386
Preprint. Discussion started: 4 August 2026

3.3.3 Plume-aligned concentration-ridge spacing

Multiple resolved concentration ridges were detected in only 2 of the 24 Scenario II profiles evaluated across the three relative progress levels (Table S6). Under the TO, TT, and TH settings, all HD and ND profiles contained fewer than two resolved peaks, and the corresponding spacing metrics were therefore undefined. The two multi-ridge profiles occurred under the DT setting. At the 0.25 progress level, DTHD contained two resolved ridges with a characteristic spacing of 1.3×10^{-3} m. At the 0.60 level, DTND contained five resolved ridges with a median adjacent-ridge spacing of 1.8×10^{-4} m and an interquartile range of 3.5×10^{-4} m. No multi-ridge profile was detected at the 1.00 progress level.

Multi-ridge organization was therefore localized and stage-dependent rather than a general feature of Scenario II. Given this limited occurrence, the ridge analysis did not support a general HD–ND channelization contrast and was retained only as a supplementary descriptor of localized plume structure.

4 Discussion

4.1 Relative roles of the interfacial electrochemical setting and pore architecture

Across the tested case matrix, the interfacial electrochemical setting determined the broad magnitude and timescale of CMZ tracer depletion, whereas pore architecture redistributed the resulting transport through the pore space. Under the common 10 mM background electrolyte condition, the implemented EDL formulation produced faster CMZ depletion and weaker late-time persistence than the ETL formulation. Within the ETL formulation, increasing C_b progressively reduced depletion and enhanced tracer persistence. These group-level contrasts were consistently larger than the differences among pore geometries within each group, indicating that the overall transport regime was primarily governed by the chemistry-dependent interfacial response.

Pore architecture nevertheless modified transport within each regime. Packing orientation and composite organization affected threshold-attainment times, directional velocity partitioning, plume orientation, anisotropy, and centroid motion. The interfacial setting and pore structure therefore acted at distinct but coupled levels: the former determined the available electroosmotic mobility and characteristic transport timescale, whereas the latter distributed the resulting flow among alternative directions and pathways. This distinction also explains why fixed-time CMZ metrics and spatial plume descriptors highlighted different structural contrasts: they characterize different aspects and stages of transport.

4.2 Chemistry–interface–transport coupling

The group-level differences arose from the dynamic coupling among electrode-driven aqueous chemistry, interfacial charge, and porewater transport (Fig. 13). Electrolysis modified pH and ionic composition at the lateral boundaries, while electromigration and advection propagated these changes through the pore space. The evolving aqueous conditions updated the local zeta potential and electroosmotic mobility, thereby modifying the tangential slip velocity and resulting porewater

https://doi.org/10.5194/egusphere-2026-4386
Preprint. Discussion started: 4 August 2026

flow. The flow, in turn, redistributed H^+, OH^-, and the background ions. The simulations thus resolve a transient feedback pathway linking boundary chemistry, interfacial electrokinetics, and solute transport, consistent with previous evidence that electroosmotic mobility depends strongly on porewater pH and electrolyte conditions (Eykholt and Daniel, 1994; Dzenitis, 1997; Sprocati et al., 2021).

Under the common 10 mM electrolyte condition, the implemented EDL formulation predicted a more negative zeta potential and greater electroosmotic mobility than the ETL formulation, consistent with the faster depletion and weaker tailing in the DT cases. Within the ETL formulation, increasing electrolyte concentration reduced the magnitude of the predicted zeta potential and electroosmotic mobility, producing the TO–TT–TH ordering in porewater speed and CMZ persistence. In the selected ETL closure, this concentration dependence reflects the representation of specific cation adsorption, interfacial charge partitioning, and the resulting shear-plane potential. Propagation of these interfacial differences through the electroosmotic-slip relation generated persistent contrasts in pore-scale flow and tracer displacement.

Because the EDL and ETL formulations contain different constitutive assumptions and parameter sets, their comparison should be interpreted as evidence that transient transport predictions are sensitive to the selected interfacial representation, rather than as a universal ranking of model accuracy. Independent measurements of transient zeta potential and electroosmotic flux would be needed to determine which formulation is more appropriate for a particular mineral–electrolyte system.

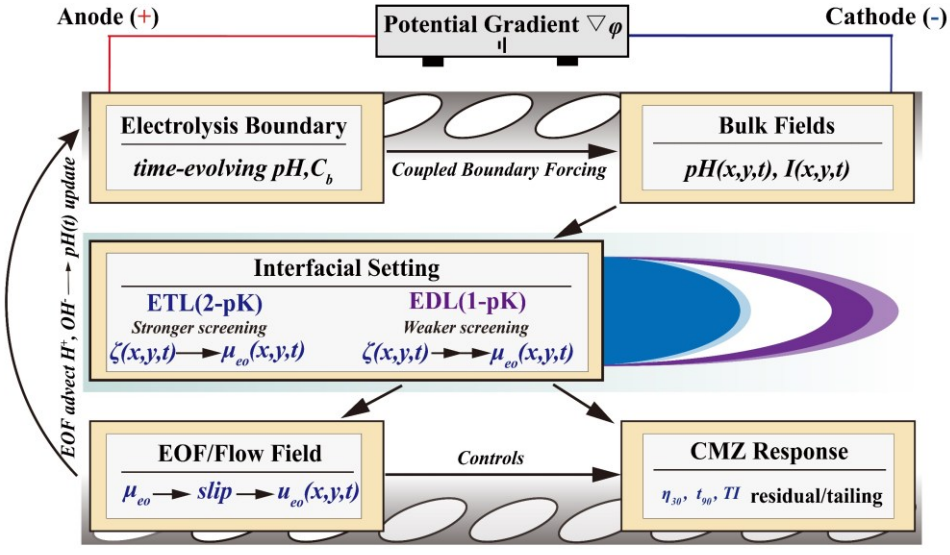

Figure 13. Conceptual synthesis of the coupled pathway from electrolysis-driven boundary chemistry to interfacial-charge regulation, electroosmotic mobility, porewater flow, and CMZ tracer depletion. Pore architecture redistributes the resulting flow and controls plume organization within the pore space.

4.3 Structural controls on directional transport and plume organization

In Scenario I, packing rotation redistributed the tangential electric field and electroosmotic slip between the applied-field and transverse directions. As the SROE angle increased, the gradient-aligned components generally decreased, whereas the

https://doi.org/10.5194/egusphere-2026-4386
Preprint. Discussion started: 4 August 2026

transverse components increased from approximately zero. This response is consistent with the changing projection of the electric field along rotated grain surfaces and the resulting redistribution of interfacial slip. Similar effects of pore geometry on electrokinetic flow and dispersion have been reported in previous pore-scale studies (Hlushkou et al., 2007; Alizadeh et al., 2019; Godinez-Brizuela and Niasar, 2020).

These changes in directional flow partitioning produced a non-monotonic response in CMZ-scale depletion. Across the TO, TT, and DT groups, the 30° geometry showed the most favourable combination of CMZ metrics, with the greatest 30 min depletion, the shortest $t_{90,\mathrm{CMZ}}$, and the lowest or joint-lowest tailing index. The TH group showed the same structural tendency in the available fixed-window metrics, with TH30 exhibiting the greatest depletion and the lowest tailing index, although all TH cases remained right-censored for $t_{90,\mathrm{CMZ}}$. Because electroosmotic transport was strongly suppressed under TH, however, its CMZ depletion metrics should be interpreted cautiously and not equated directly with effective cathode-directed displacement. Thus, among the tested geometries, the 30° packing generally produced the most favourable bulk depletion response. Because only four prescribed rotation angles were evaluated and no optimization analysis was performed, this result does not establish 30° as the optimal packing angle. The observed differences in these metrics reflect the combined effects of directional velocity partitioning and rotation-induced changes in local pore-space geometry.

To distinguish these bulk transport differences from changes in plume organization, the spatial descriptors were compared at matched relative-progress levels. Increasing packing angle rotated the plume principal axis, generated transient transverse centroid displacement, and modified plume anisotropy. These contrasts remained visible at case-specific relative progress levels and were therefore not solely consequences of different transport timescales. Fixed-time and threshold-based CMZ metrics quantify bulk depletion and persistence, whereas the relative-progress descriptors show how pore structure reorganizes plume position and geometry at comparable transport stages.

The composite geometries revealed a consistent distinction in directional organization. HD maintained non-zero domain-averaged transverse electric-field and electroosmotic-slip components, reached the case-specific 0.25 and 0.60 progress levels earlier in all four electrochemical groups, and generally showed greater gradient-aligned centroid advancement at matched stages. In ND, local flow and front deformation remained evident, but the corresponding transverse components remained close to zero after domain averaging. Together, these results indicate more persistent domain-scale flow organization and earlier attainment of case-specific transport stages in HD.

This directional and timing contrast did not translate into a uniform fixed-window depletion advantage. ND showed greater 30 min depletion and weaker tailing under TO and TT, whereas HD showed greater depletion and weaker tailing under TH; under DT, both geometries approached complete depletion, with HD reaching the threshold earlier. The effect of composite organization on endpoint depletion therefore depended on the prevailing electrochemical transport regime. Because only one deterministic realization of each composite geometry was evaluated, these contrasts should be interpreted as process-based tendencies rather than a general ranking of HD and ND structures. The limited occurrence of multi-ridge profiles provided no evidence for a general geometry-dependent channelization pattern.

https://doi.org/10.5194/egusphere-2026-4386
Preprint. Discussion started: 4 August 2026

4.4 Implications and scope

These results show that transient pore-scale electrokinetic transport cannot be interpreted from either interfacial mobility or bulk depletion metrics alone. From a hydrological perspective, electroosmotically driven porewater flow is neither spatially uniform nor temporally stationary. Evolving pH and electrolyte conditions modify the interfacial mobility that controls the available flow magnitude and transport timescale, whereas pore architecture partitions the resulting porewater flow between gradient-aligned and transverse pathways. Consequently, even under a constant imposed electrical gradient, the advective capacity and direction of porewater transport can evolve over time. Fixed-time CMZ metrics are useful for quantifying depletion and persistence, whereas relative-progress plume descriptors distinguish spatial reorganization from differences in transport rate. The HD–ND comparison further shows that earlier attainment of case-specific progress levels and greater field-aligned centroid advancement need not coincide with greater end-window depletion or weaker persistence. Hydrological assessments of electrokinetically forced transport should therefore distinguish the magnitude, spatial organization, and timing of porewater flow and associated solute transport, rather than infer system behaviour from a single fixed mobility or end-window depletion metric.

These hydrological implications are most directly applicable to electrokinetically forced water and solute transport in the controlled, saturated, low-permeability porous systems examined here. Extension to natural porous media will require three-dimensional or image-based structures, structural ensembles that better separate orientation from porosity, and aqueous chemistry that accounts for non-ideal activities and relevant mineral and contaminant reactions. Measurements of transient zeta potential, electroosmotic flux, pH propagation, and tracer breakthrough would provide a direct basis for evaluating the predicted chemistry–interface–structure relationships. Within its present scope, the common simulation matrix provides a consistent basis for separating interfacial controls on transport magnitude from structural controls on flow partitioning and plume organization in low-permeability porous media.

5 Conclusions

This study examined how electrolysis-driven aqueous chemistry, interfacial-charge representation, background electrolyte concentration, and pore architecture jointly regulate transient electroosmotic transport. A common pore-scale framework was used to compare two chemistry-dependent interfacial parameterizations, an electrolyte-concentration series within the ETL formulation, and six controlled pore geometries. Fixed-time CMZ metrics were combined with stage-aligned plume descriptors to characterize transport magnitude, persistence, and spatial organization.

The interfacial electrochemical setting established the broad magnitude and timescale of electroosmotic transport. Under the common background electrolyte concentration of 10 mM, the cases using the implemented EDL parameterization showed a mean 30 min CMZ depletion fraction of 0.998 and a mean tailing index of 0.002, compared with 0.918 and 0.094 for the ETL cases. Within the ETL formulation, increasing C_b from 1 to 100 mM reduced the mean depletion fraction from 0.963 to 0.613 and increased the mean tailing index from 0.037 to 0.465; none of the 100 mM cases reached 90 % CMZ depletion within 30

https://doi.org/10.5194/egusphere-2026-4386
Preprint. Discussion started: 4 August 2026

min. These simulations show that interfacial-charge representation and electrolyte condition materially affected the predicted electroosmotic mobility, transport timescale, and late-time persistence.

Pore architecture did not overturn the overall electrochemical-group ordering but reorganized directional transport and plume geometry within each group. In the SROE geometries, packing rotation redistributed the tangential electric field and electroosmotic slip velocity from the applied-field direction towards the transverse direction, producing systematic changes in plume orientation and anisotropy but non-monotonic changes in fixed-time CMZ depletion. In the composite geometries, HD maintained stronger domain-scale directional organization, reached its case-specific early and intermediate progress levels earlier, and generally showed greater gradient-aligned centroid advancement at matched stages than ND. However, the HD–ND ranking in 30 min depletion and tailing changed with electrochemical setting, indicating that composite organization affected transport timing more consistently than endpoint depletion. Together, the results identify a two-level control on transient electroosmotic transport: evolving aqueous chemistry is translated into transport magnitude and timescale through the interfacial electrokinetic response, whereas pore structure determines how the resulting flow and solute mass are distributed through the pore space. This distinction provides a process-based basis for interpreting electrokinetically forced water movement, solute displacement, and late-time persistence in low-permeability porous media.

Code and data availability

Figure-source data, pore-scale structure files, exported COMSOL geometry files (.mphbin), and summary data and figures from the mesh- and maximum-time-step-convergence assessment are available in a private *Figshare* repository for peer review (Wu et al., 2026; https://figshare.com/s/c705e08395c02dc48375). The archived materials support verification of the reported figures, simulation geometries, and numerical-convergence assessment. COMSOL Multiphysics 5.6 and *LiveLink* for MATLAB were used for geometry transfer and numerical simulation. These proprietary software packages are available from COMSOL AB and are not redistributed. The private review link will be replaced with a public persistent DOI upon final publication.

Author contribution

PY and WW conceptualized the study. PY developed the model. WW and PY performed the simulations, curated the data, and prepared the visualizations. WW, GP, HD, JY, and PY conducted the formal analysis and interpreted the results. PY and WW acquired funding. WW, PY, and GP prepared the original draft. PY, HD, and JY reviewed and edited the manuscript. All authors approved the final manuscript.

https://doi.org/10.5194/egusphere-2026-4386
Preprint. Discussion started: 4 August 2026

Competing interests

The authors declare that they have no conflict of interest. Heng Dai is a member of the editorial board of Hydrology and Earth System Sciences.

Disclaimer

Copernicus Publications remains neutral with regard to jurisdictional claims made in the text, published maps, institutional affiliations, or any other geographical representation in this paper. While Copernicus Publications makes every effort to include appropriate place names, the final responsibility lies with the authors. Views expressed in the text are those of the authors and do not necessarily reflect the views of the publisher.

Acknowledgements

The authors acknowledge the High-Performance Computing Center of Nanjing University for providing the computational resources used in this study. ChatGPT (OpenAI) was used to assist with English-language editing and to improve readability. All scientific content, analyses, interpretations, and final wording were reviewed and approved by the authors.

Financial support

This research has been supported by the National Key Research and Development Program of China (grant no. 2023YFC3709700), the National Natural Science Foundation of China (grant no. 42407123), and the Basic and Applied Basic Research Foundation of Guangdong Province (grant no. 2023A1515110358).

References

Acar, Y. B. and Alshawabkeh, A. N.: Principles of electrokinetic remediation, Environ. Sci. Technol., 27, 2638-2647, 10.1021/es00049a002, 1993.

Alizadeh, A., Jin, X., and Wang, M. R.: Pore-scale study of ion transport mechanisms in inhomogeneously charged nanoporous rocks: Impacts of interface properties on macroscopic transport, J. Geophys. Res.: Solid Earth, 124, 5387-5407, 10.1029/2018jb017200, 2019.

Alizadeh, A., Warkiani, M. E., and Wang, M. R.: Manipulating electrokinetic conductance of nanofluidic channel by varying inlet pH of solution, Microfluid. Nanofluid., 21, 15, 10.1007/s10404-017-1892-9, 2017.

Appelo, C. A. J.: Solute transport solved with the Nernst-Planck equation for concrete pores with 'free' water and a double layer, Cem. Concr. Res., 101, 102-113, 10.1016/j.cemconres.2017.08.030, 2017.

https://doi.org/10.5194/egusphere-2026-4386
Preprint. Discussion started: 4 August 2026

Boso, F., de Barros, F., Fiori, A., and Bellin, A.: Performance analysis of statistical spatial measures for contaminant plume characterization toward risk-based decision making, Water Resour. Res., 49, 3119-3132, 10.1002/wrcr.20270, 2013.

Bray, A. W., Benning, L. G., Bonneville, S., and Oelkers, E. H.: Biotite surface chemistry as a function of aqueous fluid composition, Geochimica et Cosmochimica Acta, 128, 58-70, 10.1016/j.gca.2013.12.002, 2014.

Cang, L., Fan, G. P., Zhou, D. M., and Wang, Q. Y.: Enhanced-electrokinetic remediation of copper-pyrene co-contaminated soil with different oxidants and pH control, Chemosphere, 90, 2326-2331, 10.1016/j.chemosphere.2012.10.062, 2013.

Chowdhury, A. I. A., Gerhard, J. I., Reynolds, D., and O'Carroll, D. M.: Low permeability zone remediation via oxidant delivered by electrokinetics and activated by electrical resistance heating: Proof of Concept, Environ. Sci. Technol., 51, 13295-13303, 10.1021/acs.est.7b02231, 2017.

Crespy, A., Boleve, A., and Revil, A.: Influence of the Dukhin and Reynolds numbers on the apparent zeta potential of granular porous media, J. Colloid Interface Sci., 305, 188-194, 10.1016/j.jcis.2006.09.038, 2007.

de Barros, F., Fernàndez-Garcia, D., Bolster, D., and Sanchez-Vila, X.: A risk-based probabilistic framework to estimate the endpoint of remediation: Concentration rebound by rate-limited mass transfer, Water Resour. Res., 49, 1929-1942, 10.1002/wrcr.20171, 2013.

de Barros, F., Bellin, A., Cvetkovic, V., Dagan, G., and Fiori, A.: Aquifer heterogeneity controls on adverse human health effects and the concept of the hazard attenuation factor, Water Resour. Res., 52, 5911-5922, 10.1002/2016WR018933, 2016.

de Dreuzy, J., Carrera, J., Dentz, M., and Le Borgne, T.: Time evolution of mixing in heterogeneous porous media, Water Resour. Res., 48, 10.1029/2011WR011360, 2012.

de Lima, S. A., Murad, M. A., Moyne, C., and Stemmelen, D.: A three-scale model of pH-dependent flows and ion transport with equilibrium adsorption in kaolinite clays: I. Homogenization analysis, Transp. Porous Media, 85, 23-44, 10.1007/s11242-010-9545-4, 2010a.

de Lima, S. A., Murad, M. A., Moyne, C., Stemmelen, D., and Boutin, C.: A three-scale model of pH-dependent flows and ion transport with equilibrium adsorption in kaolinite clays: II Effective-medium behavior, Transp. Porous Media, 85, 45-78, 10.1007/s11242-010-9546-3, 2010b.

Dzenitis, J. M.: Soil chemistry effects and flow prediction in electroremediation of soil, Environ. Sci. Technol., 31, 1191-1197, 10.1021/es960707e, 1997.

Eykholt, G. R. and Daniel, D. E.: Impact of system chemistry on electroosmosis in contaminated soil, J. Geotech. Eng.-ASCE, 120, 797-815, 10.1061/(asce)0733-9410(1994)120:5(797), 1994.

Fiori, A.: Channeling, channel density and mass recovery in aquifer transport, with application to the MADE experiment, Water Resour. Res., 50, 9148-9161, 10.1002/2014WR015950, 2014.

Gill, R. T., Harbottle, M. J., Smith, J. W. N., and Thornton, S. F.: Electrokinetic-enhanced bioremediation of organic contaminants: A review of processes and environmental applications, Chemosphere, 107, 31-42, 10.1016/j.chemosphere.2014.03.019, 2014.

https://doi.org/10.5194/egusphere-2026-4386
Preprint. Discussion started: 4 August 2026

Godinez-Brizuela, O. E. and Niasar, V. J.: Simultaneous pressure and electro-osmosis driven flow in charged porous media: Pore-scale effects on mixing and dispersion, J. Colloid Interface Sci., 561, 162-172, 10.1016/j.jcis.2019.11.084, 2020.

Hlushkou, D., Khirevich, S., Apanasovich, V., Seidel-Morgenstern, A., and Tallarek, U.: Pore-scale dispersion in electrokinetic flow through a random sphere packing, Anal. Chem., 79, 113-121, 10.1021/ac061168r, 2007.

Hyman, J.: Flow Channeling in Fracture Networks: Characterizing the Effect of Density on Preferential Flow Path Formation, Water Resour. Res., 56, 10.1029/2020WR027986, 2020.

Jiménez-Martínez, J., Le Borgne, T., Tabuteau, H., and Méheust, Y.: Impact of saturation on dispersion and mixing in porous media: Photobleaching pulse injection experiments and shear-enhanced mixing model, Water Resour. Res., 53, 1457-1472, 10.1002/2016WR019849, 2017.

Ko, S. O., Schlautman, M. A., and Carraway, E. R.: Cyclodextrin-enhanced electrokinetic removal of phenanthrene from a model clay soil, Environ. Sci. Technol., 34, 1535-1541, 10.1021/es990223t, 2000.

Leroy, P., Revil, A., Altmann, S., and Tournassat, C.: Modeling the composition of the pore water in a clay-rock geological formation (Callovo-Oxfordian, France), Geochimica et Cosmochimica Acta, 71, 1087-1097, 10.1016/j.gca.2006.11.009, 2007.

Li, W. W. and Yu, H. Q.: Electro-assisted groundwater bioremediation: Fundamentals, challenges and future perspectives, Bioresour. Technol., 196, 677-684, 10.1016/j.biortech.2015.07.074, 2015.

Lide, D. R.: CRC Handbook of Chemistry and Physics, 83rd Edition, Crc Handbook of Chemistry & Physics, 504, 2002.

Liu, Y. J., Naidu, R., and Ming, H.: Surface electrochemical properties of red mud (bauxite residue): Zeta potential and surface charge density, J. Colloid Interface Sci., 394, 451-457, 10.1016/j.jcis.2012.11.052, 2013.

Lopez-Vizcaino, R., Yustres, A., Leon, M. J., Saez, C., Canizares, P., Rodrigo, M. A., and Navarro, V.: Multiphysics implementation of electrokinetic remediation models for natural soils and porewaters, Electrochim. Acta, 225, 93-104, 10.1016/j.electacta.2016.12.102, 2017.

Masi, M., Ceccarini, A., and Iannelli, R.: Multispecies reactive transport modelling of electrokinetic remediation of harbour sediments, J. Hazard. Mater., 326, 187-196, 10.1016/j.jhazmat.2016.12.032, 2017.

Palodhi, L. and Mishra, M.: Concentration-dependent diffusion effects on miscible radial viscous fingering, Phys. Fluids, 37, 10.1063/5.0285763, 2025.

Papirer, E.: Adsorption on Silica Surfaces, Adsorption on Silica Surfaces, New York2000.

Peters, P. B., van Roij, R., Bazant, M. Z., and Biesheuvel, P. M.: Analysis of electrolyte transport through charged nanopores, Phys. Rev. E, 93, 14, 10.1103/PhysRevE.93.053108, 2016.

Qiao, W. J., Ye, S. J., Wu, J. C., and Zhang, M.: Surfactant-enhanced electroosmotic flushing in a tricholrobenzene contaminated clayey soil, Groundwater, 56, 673-679, 10.1111/gwat.12631, 2018.

Qin, J. Y., Sun, X. H., Liu, Y., Berthold, T., Harms, H., and Wick, L. Y.: Electrokinetic control of bacterial deposition and transport, Environ. Sci. Technol., 49, 5663-5671, 10.1021/es506245y, 2015.

Revil, A.: Transport of water and ions in partially water-saturated porous media. Part 1. Constitutive equations, Adv. Water Resour., 103, 119-138, 10.1016/j.advwatres.2016.02.006, 2017.

https://doi.org/10.5194/egusphere-2026-4386
Preprint. Discussion started: 4 August 2026

Rezaee, M., Asadollahfardi, G., Gomez-Lahoz, C., Villen-Guzman, M., and Paz-Garcia, J. M.: Modeling of electrokinetic remediation of Cd- and Pb-contaminated kaolinite, J. Hazard. Mater., 366, 630-635, 10.1016/j.jhazmat.2018.12.034, 2019.

Shapiro, A. P. and Probstein, R. F.: Removal of contaminants from saturated clay by electroosmosis, Environ. Sci. Technol., 27, 283-291, 10.1021/es00039a007, 1993.

Shi, L., Harms, H., and Wick, L. Y.: Electroosmotic flow stimulates the release of alginate-bound phenanthrene, Environ. Sci. Technol., 42, 2105-2110, 10.1021/es702357p, 2008.

Sole-Mari, G., Fernàndez-Garcia, D., Sanchez-Vila, X., and Bolster, D.: Lagrangian Modeling of Mixing-Limited Reactive Transport in Porous Media: Multirate Interaction by Exchange With the Mean, Water Resour. Res., 56, 10.1029/2019WR026993, 2020.

Souza, F. L., Saez, C., Lanza, M. R. V., Canizares, P., and Rodrigo, M. A.: Removal of chlorsulfuron and 2,4-D from spiked soil using reversible electrokinetic adsorption barriers, Sep. Purif. Technol., 178, 147-153, 10.1016/j.seppur.2017.01.030, 2017.

Sprocati, R., Flyvbjerg, J., Tuxen, N., and Rolle, M.: Process-based modeling of electrokinetic-enhanced bioremediation of chlorinated ethenes, J. Hazard. Mater., 397, 14, 10.1016/j.jhazmat.2020.122787, 2020.

Sprocati, R., Gallo, A., Sethi, R., and Rolle, M.: Electrokinetic delivery of reactants: Pore water chemistry controls transport, mixing, and degradation, Environ. Sci. Technol., 55, 719-729, 10.1021/acs.est.0c06054, 2021.

Sprocati, R., Masi, M., Muniruzzaman, M., and Rolle, M.: Modeling electrokinetic transport and biogeochemical reactions in porous media: A multidimensional Nernst-Planck-Poisson approach with PHREEQC coupling, Adv. Water Resour., 127, 134-147, 10.1016/j.advwatres.2019.03.011, 2019.

Sun, Z. C., Wu, B., Guo, P. H., Wang, S., and Guo, S. H.: Enhanced electrokinetic remediation and simulation of cadmium-contaminated soil by superimposed electric field, Chemosphere, 233, 17-24, 10.1016/j.chemosphere.2019.05.233, 2019.

Thormann, W., Zhang, C. X., Caslavska, J., Gebauer, P., and Mosher, R. A.: Modeling of the impact of ionic strength on the electroosmotic flow in capillary electrophoresis with uniform and discontinuous buffer systems, Anal. Chem., 70, 549-562, 10.1021/ac970513x, 1998.

Vizcaino, R. L., Yustres, A., Asensio, L., Saez, C., Canizares, P., Rodrigo, M. A., and Navarro, V.: Enhanced electrokinetic remediation of polluted soils by anolyte pH conditioning, Chemosphere, 199, 477-485, 10.1016/j.chemosphere.2018.02.038, 2018.

Wang, M. and Revil, A.: Electrochemical charge of silica surfaces at high ionic strength in narrow channels, J. Colloid Interface Sci., 343, 381-386, 10.1016/j.jcis.2009.11.039, 2010.

Wu, W., Pan, G., Dai, H., Yang, J., and Yang, P.: Source data, pore-scale structure files, geometry-generation outputs, and numerical-convergence results for “Transient electroosmotic transport under evolving pH and contrasting background electrolyte concentrations: coupled controls of interfacial charge and pore structure”, *Figshare [data set and code]*, https://figshare.com/s/c705e08395c02dc48375, 2026.

Xu, H. T., Song, Y., Cang, L., and Zhou, D. M.: Ion exchange membranes enhance the electrokinetic in situ chemical oxidation of PAH-contaminated soil, J. Hazard. Mater., 382, 9, 10.1016/j.jhazmat.2019.121042, 2020.

https://doi.org/10.5194/egusphere-2026-4386
Preprint. Discussion started: 4 August 2026

Xu, J. W., Liu, C., Hsu, P. C., Zhao, J., Wu, T., Tang, J., Liu, K., and Cui, Y.: Remediation of heavy metal contaminated soil by asymmetrical alternating current electrochemistry, Nat. Commun., 10, 8, 10.1038/s41467-019-10472-x, 2019.

Yang, P., Ye, S. J., Wu, J. F., and Wu, J. C.: Process-based pore-scale simulation of electrokinetic remediation of organic pollutant in porous media, J. Hydrol., 613, 15, 10.1016/j.jhydrol.2022.128436, 2022.

Yang, Y. K. and Wang, M. R.: Cation diffusion in compacted clay: A pore-scale view, Environ. Sci. Technol., 53, 1976-1984, 10.1021/acs.est.8b05755, 2019.

Yeung, A. T. and Datla, S.: Fundamental formulation of electrokinetic extraction of contaminants from soil, Can. Geotech. J., 32, 569-583, 10.1139/t95-060, 1995.

Yeung, A. T. and Gu, Y. Y.: A review on techniques to enhance electrochemical remediation of contaminated soils, J. Hazard. Mater., 195, 11-29, 10.1016/j.jhazmat.2011.08.047, 2011.

Zhang, H. and Zhang, X. N.: Electrokinetic properties of ferralsols in china in relation to pedogenic development, Geoderma, 54, 173-188, 1992.

Zhang, L. and Wang, M. R.: Modeling of electrokinetic reactive transport in micropore using a coupled lattice Boltzmann method, J. Geophys. Res.: Solid Earth, 120, 2877-2890, 10.1002/2014jb011812, 2015.

Zhang, L. and Wang, M. R.: Electro-osmosis in inhomogeneously charged microporous media by pore-scale modeling, J. Colloid Interface Sci., 486, 219-231, 10.1016/j.jcis.2016.09.057, 2017.